Monthly Notices of the ROYAL ASTRONOMICAL SOCIETY

MNRAS **530,** 1829–1848 (2024) https://doi.org/10.1093/mnras/stae789
Advance Access publication 2024 March 19

E-XQR-30: The evolution of Mg II, C II, and O I across $2 < z < 6$

Alma Maria Sebastian [1,2★] Emma Ryan-Weber,[1,2★] Rebecca L. Davies,[1,2★] George D. Becker,[3] Laura C. Keating [4] Valentina D'Odorico [5,6,7] Romain A. Meyer [8] Sarah E. I. Bosman [9,10] Guido Cupani [5,7] Girish Kulkarni [11] Martin G. Haehnelt,[12] Samuel Lai,[13] Anna–Christina Eilers [14] Manuela Bischetti[15] and Simona Gallerani[6]

[1]*Centre for Astronomy and Astrophysics, Swinburne University of Technology, Hawthorn, Victoria 3122, Australia*
[2]*ARC Centre of Excellence for All Sky Astrophysics in 3 Dimensions (ASTRO3D), Canberra, ACT 2611, Australia*
[3]*Department of Physics & Astronomy, University of California, Riverside, CA 92521, USA*
[4]*Institute for Astronomy, University of Edinburgh, Blackford Hill, Edinburgh EH9 3HJ, UK*
[5]*INAF-Osservatorio Astronomico di Trieste, via G. Tiepolo 11, I-34143 Trieste, Italy*
[6]*Scuola Normale Superiore, Piazza dei Cavalieri, I-56126 Pisa, Italy*
[7]*IFPU–Institute for Fundamental Physics of the Universe, via Beirut 2, I-34151 Trieste, Italy*
[8]*Department of Astronomy, University of Geneva, Chemin Pegasi 51, CH-1290 Versoix, Switzerland*
[9]*Institute for Theoretical Physics, Heidelberg University, Philosophenweg 12, D-69120 Heidelberg, Germany*
[10]*Galaxies and Cosmolgy Department, Max Planck Institut für Astronomie, Königstuhl 17, D-69117 Heidelberg, Germany*
[11]*Department of Theoretical Physics, Tata Institute of Fundamental Research, Homi Bhabha Road, Mumbai 400005, India*
[12]*Kavli Institute for Cosmology and Institute of Astronomy, Madingley Road, Cambridge CB3 0HA, UK*
[13]*Research School of Astronomy and Astrophysics, Australian National University, Canberra, ACT 2611, Australia*
[14]*MIT Kavli Institute for Astrophysics and Space Research, Massachusetts Institute of Technology, Cambridge, MA 02139, USA*
[15]*Dipartimento di Fisica, Università di Trieste, Sezione di Astronomia, Via G.B. Tiepolo 11, I-34131 Trieste, Italy*

Accepted 2024 March 14. Received 2024 March 11; in original form 2023 October 16

ABSTRACT

Intervening metal absorbers in quasar spectra at $z > 6$ can be used as probes to study the chemical enrichment of the Universe during the Epoch of Reionization. This work presents the comoving line densities (dn/dX) of low-ionization absorbers, namely, Mg II (2796 Å), C II (1334 Å), and O I (1302 Å) across $2 < z < 6$ using the E-XQR-30 metal absorber catalogue prepared from 42 XSHOOTER quasar spectra at $5.8 < z < 6.6$. Here, we analyse 280 Mg II ($1.9 < z < 6.4$), 22 C II ($5.2 < z < 6.4$), and 10 O I ($5.3 < z < 6.4$) intervening absorbers, thereby building up on previous studies with improved sensitivity of 50 per cent completeness at an equivalent width of $W > 0.03$ Å. For the first time, we present the comoving line densities of 131 weak ($W < 0.3$ Å) intervening Mg II absorbers at $1.9 < z < 6.4$ which exhibit constant evolution with redshift similar to medium ($0.3 < W < 1.0$ Å) absorbers. However, the cosmic mass density of Mg II – dominated by strong Mg II systems – traces the evolution of global star formation history from redshift 1.9 to 5.5. E-XQR-30 also increases the absorption path-length by a factor of 50 per cent for C II and O I whose line densities show a rising trend towards $z > 5$, in agreement with previous works. In the context of a decline in the metal enrichment of the Universe at $z > 5$, the overall evolution in the incidence rates of absorption systems can be explained by a weak – possibly soft fluctuating – ultraviolet background. Our results, thereby, provide evidence for a late reionization continuing to occur in metal-enriched and therefore, biased regions in the Universe.

Key words: galaxies: haloes – quasars: absorption lines – early Universe.

1 INTRODUCTION

The Epoch of Reionization (EoR) marks a major transition in the evolutionary history of the Universe when cosmic neutral hydrogen was (re)ionized by ultraviolet (UV) radiation from the first light sources and thereby marked an end to the Dark Ages. Studying reionization involves the understanding of the nature, formation and evolution of the first generation of stars and galaxies, quasars and the nature of the ionizing radiation. The theoretical and observational consensus view on the process of EoR indicates a patchy reionization with photoionized bubbles starting out in the vicinity of ionizing sources, which then expand and overlap, thus ionizing the whole Universe (Loeb & Barkana 2001; Furlanetto & Oh 2005; Oppenheimer, Davé & Finlator 2009; Becker, Bolton & Lidz 2015a; Bosman et al. 2022). Studies using Lyman α optical depth measurements in high-redshift quasar spectra (Fan et al. 2006; Becker et al. 2015b; Eilers, Davies & Hennawi 2018; Yang et al. 2020; Choudhury, Paranjape & Bosman 2021; Bosman et al. 2022), dark gap statistics in Lyman α forest (Songaila & Cowie 2002; Furlanetto, Hernquist & Zaldarriaga 2004; Gallerani et al. 2008; Gnedin, Becker & Fan 2017; Nasir & D'Aloisio

★ E-mail: asebastian@swin.edu.au (AMS); eryanweber@swin.edu.au (ERW); rdavies@swin.edu.au (RLD)

2020; Zhu et al. 2021, 2022) and Lyman α damping wing absorption (Bañados et al. 2018; Davies et al. 2018; Wang et al. 2020; Greig et al. 2022) propose a late end to the EoR towards $z < 6$. The same sources of ionizing radiation polluted the Universe with elements heavier than hydrogen and helium produced during stellar nucleosynthesis by ejecting them into the surrounding interstellar, circumgalactic, and intergalactic media (ISM, CGM, and IGM) through stellar and galactic feedback processes.

The CGM is the multiphase gas surrounding galaxies that extends from their disks to the virial radii and acts as a resource for star formation fuel and a venue for galactic feedback and recycling (Tumlinson, Peeples & Werk 2017). Metals in the CGM offer many important insights into the evolutionary histories of their host galaxies. The quantity of metals depends on the past rate of metal ejection by outflows, and the ionization state of the metals can provide a key probe of the ionizing photon background. At large radii, the CGM is ionized by UV radiation from external sources rather than from the host galaxy: the metals in the diffuse medium will exhibit a transition in their ionization state with respect to the intensity of the ionizing background. Therefore, metal absorbers in galaxy haloes at high redshifts can be used to study the ionization state of the gas near the EoR. Moreover, the ionizing UV background evolves to a softer spectrum with redshift as the population of luminous active galactic nuclei (AGN) decline towards redshift $z > 5$ (Becker & Bolton 2013; D'Aloisio et al. 2017; Kulkarni, Worseck & Hennawi 2019; Faucher-Giguère 2020). As a result, we would expect the outer parts of the CGM that are exposed to the ionizing background to undergo a transition in their ionization state.

Quasar absorption spectroscopy is an effective method for detecting absorbers that reside in low-density gas such as CGM and IGM and at high redshift that are beyond the detection threshold of emission-line surveys (Becker et al. 2015a; Péroux & Howk 2020).

The observations independently probe the global star formation history (SFH; Ménard et al. 2011; Matejek & Simcoe 2012; Madau & Dickinson 2014; Chen et al. 2017). Conventionally, the metal abundance of a galaxy or gas cloud is expressed in metallicity, given by the ratio of metals to neutral hydrogen. However, at $z > 5$, due to the saturation of the Lyman α forest, it is difficult to measure H I absorbers in the quasar spectra. As a result, observers use low-ionization metal absorbers as probes for neutral hydrogen at high z. They are metal absorbers with ionization potentials less than neutral hydrogen (13.6 eV) (e.g. O I, C II, Si II, etc.) and, therefore, can be used to trace neutral regions of CGM or IGM (Furlanetto & Oh 2005; Oppenheimer et al. 2009; Keating et al. 2014; Finlator et al. 2016).

Studies of Mg II absorbers at redshifts $z < 2$ based on their equivalent widths show that medium ($0.3 < W < 1.0$ Å) and strong ($W > 1.0$ Å) Mg II trace cool regions of outflows from blue star-forming galaxies and thereby following the global SFH (Prochter, Prochaska & Burles 2006; Zibetti et al. 2007; Lundgren et al. 2009; Weiner et al. 2009; Noterdaeme, Srianand & Mohan 2010; Rubin et al. 2010; Bordoloi et al. 2011; Ménard et al. 2011; Nestor et al. 2011). Meanwhile, works by Kacprzak et al. (2011), Kacprzak, Churchill & Nielsen (2012), and Nielsen et al. (2015) indicate that weak Mg II absorbers ($W < 0.3$ Å) trace the corotating and infalling gas in the CGM. There can be significant variations in star formation rates, metal enrichment rate and halo assembly with lookback time and therefore it is necessary to extend the studies of Mg II systems beyond the peak of cosmic star formation rate at $z \sim 2.5-3$ (Madau & Dickinson 2014) to understand galaxy transformation across different epochs. The first high redshift $z \sim 6$ survey of Mg II was conducted by Matejek & Simcoe (2012) over $2.5 < z < 6$ using the Folded-port InfraRed Echellette (FIRE) spectrograph on Magellan. Further work by Chen et al. (2017) added sightlines across $2 < z < 7$. Both works show that the incidence rates of strong Mg II absorbers decline with redshift following the cosmic SFH while those of weaker absorbers remain constant with increasing redshift.

Meanwhile, several works were conducted on $z < 3$ weak Mg II absorbers after their detection by Tripp, Lu & Savage (1997) and Churchill et al. (1999) to study their properties (see Rigby, Charlton & Churchill 2002; Churchill, Kacprzak & Steidel 2005; Lynch & Charlton 2007; Narayanan et al. 2007, 2008; Mathes, Churchill & Murphy 2017; Muzahid et al. 2018). These low-redshift studies on weak Mg II inferred that they arose from sub-Lyman Limit systems (sub-LLS having $\log N_{\rm H\,I}/{\rm cm}^2 < 17.2$) with supersolar metallicity. Mathes et al. (2017) predicted that the weak Mg II absorbers should not be detected at $z > 3.3$ based on their number density statistics. Nevertheless, Chen et al. (2017) detected some weak Mg II absorbers at $2 < z < 7$, but with low completeness, demonstrating the potential for near-IR instruments with improved sensitivity and resolution to detect more weak Mg II systems.

Theoretical studies on $z > 5$ have indicated that dense neutral regions that have been polluted by metals will give rise to forests of low-ionization absorption lines such as C II and O I (Oh 2002). Furlanetto & Loeb (2003) using their supernova wind model, argued that a substantial fraction of the metals in high-redshift galactic superwinds which polluted the IGM existed as low-ionization absorbers (LIAs) like C II, O I, Si II, and Fe II. Using a self-consistent multifrequency UV model involving well-constrained galactic outflows, Finlator et al. (2015) show that the C II mass fraction should drop towards lower redshifts relative to the increase in C IV towards $z \lesssim 6$. Simulations to model the reionization of the metal-enriched CGM at $z \sim 6$ in Keating et al. (2014) and Doughty & Finlator (2019) predict a rapid evolution of O I at $z > 5$ that probe regions of neutral hydrogen at these redshifts.

Observations by Cooper et al. (2019) using 69 intervening systems from Magellan/FIRE and Keck/HIRES find that the column density ratios of C II/C IV increase towards $z > 5$ which could be due to the combined effect of lower chemical abundance and softer ionizing background at $z \sim 6$. Similar results can be seen in Becker et al. (2006, 2011) where there is a high number density of LIAs such as C II and O I at $z \sim 6$. The first self consistent survey for O I absorbers using a larger number of sightlines (199) on Keck/ESI and Very Large Telescope (VLT)/XSHOOTER was conducted by Becker et al. (2019). They found an upturn in the O I comoving line density at $z > 5.7$, which they interpreted as an evolution in the ionization of metal-enriched gas, with lower ionization states being more common at $z \sim 6$ than at $z \sim 5$. Additionally, studies on C IV at $z > 5$ (e.g. D'Odorico et al. 2010, 2013; Davies et al. 2023b) show the declining trend in absorption path density or mass density of highly ionized carbon with increasing redshift. Finlator et al. (2016), comparing the existing observational data from Becker et al. (2011) and D'Odorico et al. (2013) with their models for different UV backgrounds, demonstrate that a softer fluctuating UV background reproduces the observed Si IV/C IV and C II/C IV distributions.

In general, the increasing trend observed in LIAs and the decline in the incidence rates of high-ionization absorbers point to a phase transition occurring in the CGM and IGM at $z > 5$. Considering the metal absorbers as potential tracers of the host galaxies from which they are ejected, they can provide information about the relation between the galaxies and the absorbers, the environments in which they arise as well as the factors that drive their evolution. Furthermore, reionization models have not been fully successful in reproducing the observed trends in metal absorbers redshift evolution (e.g. Finlator et al. 2016; Keating et al. 2016; Doughty & Finlator

2019). More observational constraints along with cosmological hydrodynamic simulations are required to improve our understanding of the reionization history of the Universe.

In particular, deeper observations over a larger number of sight-lines are required to better characterize the evolution of metal absorbers and to understand how the metal content and ionization state of galaxy haloes are impacted by reionization. This paper uses data from the ESO VLT Large Program – the Ultimate XSHOOTER legacy survey of quasars at $z \sim 5.8-6.6$ (XQR-30, D'Odorico et al. 2023). XQR-30 is a spectroscopic survey of 30 (+12 from the archive and therefore, enlarged XQR-30 or E-XQR-30) quasars at high redshifts in the optical and near-infrared wavelength range (3000–25000 Å) using the XSHOOTER spectrograph (Vernet et al. 2011) at the European Southern Observatory (ESO) VLT. The archival observations of quasars from XSHOOTER have the same magnitude and redshift range as that of XQR-30 quasars with similar resolution and signal-to-noise ratio (S/N). The E-XQR-30 quasar spectra have an intermediate resolution of $R \sim 10000$ and a minimum (median) S/N of 10 (∼29) per 10 km s^{-1} spectral pixel at a rest wavelength of 1258 Å (D'Odorico et al. 2023). The primary aim of this work is to understand the evolution of CGM absorbers at $z > 5$ and the nature, particularly the strength, of ionizing photons towards the tail end of the EoR. This study is also important in the light of the recent revival of the possibility of quasars contributing significantly to the UV background at $z \sim 6$ (Grazian et al. 2023; Harikane et al. 2023; Maiolino et al. 2023). E-XQR-30 has already been used to constrain the end of EoR (Zhu et al. 2021; Bosman et al. 2022), studying the early quasars and their environment (Bischetti et al. 2022) as well as the evolution of high-ionization absorbers like C IV (Davies et al. 2023b).

The metal absorber data used in this study are obtained from the E-XQR-30 metal absorber catalogue (Davies et al. 2023a). The catalogue has substantially increased the sample size especially for C II and weak Mg II and the path-length for the high-redshift metal absorbers such as O I and C II with deeper observations on a large number of objects and improved sensitivity of the XSHOOTER spectrograph compared to previous high-z metal absorber surveys. This paper mainly focuses on LIAs such as Mg II, C II, and O I, including the first statistical study of weak Mg II absorbers at $2 < z < 6$, and studies their redshift evolution to characterize galaxy transformation across different epochs. The results from this work are also compared to previous survey results to understand how the increased sensitivity and resolution towards high-redshift improves our understanding of the cosmic evolution of the absorbers.

The outline of the paper is as follows: Section 2 describes the E-XQR-30 metal absorber catalogue from which the data for this work are obtained and the techniques used to study the evolution of metal absorbers. We present the results of the cosmic evolution for each of the ions and their comparison with previous works in Section 3. The impacts of the observed trends in the absorber number densities with redshift are discussed in Section 4. Finally, a short summary of the entire paper is given in Section 5. Throughout this work, we adopt the ΛCDM cosmology with $H_0 = 67.7$ km s^{-1}Mpc^{-1} and $\Omega_m = 0.31$ (Planck Collaboration VI 2020).

2 METHODS

2.1 The E-XQR-30 metal absorber catalogue

The metal absorber catalogue prepared by Davies et al. (2023a) used quasar spectra from E-XQR-30 consisting of 42 quasars (D'Odorico et al. 2023). All details related to the catalogue can be found in Davies et al. (2023a) and this section summarizes some key features relevant to this work. After applying the data-reduction procedures for the 42 quasar spectra as outlined in D'Odorico et al. (2023), the spectra from each of the spectroscopic arms of XSHOOTER (VIS and NIR) were combined together into a single spectrum for each quasar. The adopted emission redshifts of each quasar were calculated from emission lines where available or from the apparent start of Lyman α forest as listed in table B1 in Davies et al. (2023a). For the preparation of the metal absorber catalogue, only absorbers redward of the Lyman α emission line and to a maximum redshift of 5000 km s^{-1} below the quasar emission redshift, were considered. The quasar spectra is completely absorbed by the Lyman α forest due to intervening neutral hydrogen so it is very challenging to search for absorption lines at wavelengths shorter than Lyman α. The wavelength regions affected by skyline or telluric contamination were excluded from the absorber search. Absorbers found in spectral regions affected by broad absorption line (BAL) troughs (Bischetti et al. 2022, 2023) were flagged in the catalogue.

The metal absorption catalogue has been prepared using an automated search for candidate systems, checking for spurious detections through customized algorithms and visual inspection and fitting of the lines with Voigt profile to obtain column density (log N) and Doppler (b) parameter. Many of the procedures used ASTROCOOK (Cupani et al. 2020), a PYTHON software for detecting and fitting quasar absorption lines.

The metal absorber components were grouped into systems using a similar method outlined in D'Odorico et al. (2022) where the components that are separated by less than 200 km s^{-1} were combined into a single system using an iterative method through the list of the systems for each line of sight. For each system, the total rest-frame equivalent width W and the W-weighted mean redshift from the constituent components were measured from the best-fitting Voigt profiles.

The absorbers are classified as proximate or intervening based on their velocity separation from quasar redshifts to avoid absorbers with ionization states or abundance patterns different from the intrinsic absorber population due to close proximity to the quasar. Based on the work of Perrotta et al. (2016), the E-XQR-30 metal absorber catalogue adopted a minimum velocity separation of 10 000 km s^{-1} from the quasar redshift to label an absorber as intervening (also known as non-proximate) along the line of sight. In this case, the maximum redshift at which an intervening ion can be detected is

$$z_{max} = (1 + z_{em}) \times \exp(-10\,000\ \mathrm{km s^{-1}}/c) - 1, \quad (1)$$

where z_{em} is the emission redshift of the quasar and c is the speed of light. Although the primary sample[1] of the E-XQR-30 catalogue adopts 10 000 km s^{-1} as the proximity limit, the published data allow users to set a different velocity threshold if desired. To this end, the work presented here also adopts the limits of 3000 and 5000 km s^{-1} to compare directly with previous works on Mg II and O I in the literature.

The evolution of the absorbers in the CGM across cosmic time can be studied by using either the individual absorption component or system data for each ion. For the purpose of this paper, only system data are considered for the redshift evolution studies of the absorbers, so that our results can be compared with previous works such as Chen et al. (2017), Cooper et al. (2019), and Becker et al. (2019) which

[1]The primary sample consists of only automatically detected systems whose completeness and false positives are well constrained.

have different spectral resolutions other than that of XSHOOTER (D'Odorico et al. 2022; Davies et al. 2023a).

The metal absorber catalogue consists of 778 systems in total including 280 Mg II, 22 C II, and 10 O I intervening systems, providing a significant increase in the number of high-redshift absorbers with high spectral resolution and S/N ratio compared to previous surveys. For example, the catalogue almost doubled the number of C II absorbers at $z > 5$ and detected a substantial population of 138 weak Mg II absorbers at $z > 2$. The E-XQR-30 sample also increases the absorption path-length for C II and O I absorbers by 50 per cent (Davies et al. 2023a) at $5.17 < z < 6.38$ in comparison to other works in the literature.

2.2 The low-ionization absorber line statistics: dn/dX

We focus on studying the evolution of LIAs, namely, Mg II, C II, and O I, across redshift using E-XQR-30 metal absorber catalogue. In order to study the change in the metal content of the galaxy haloes across redshift, we use the absorption path density (dn/dX), also known as comoving line density.[2] It gives the number of absorbers per unit absorption path-length interval. The absorption path for a given redshift is

$$X(z) = \frac{2}{3\Omega_{\rm m}}(\Omega_{\rm m}(1+z)^3 + \Omega_{\Lambda})^{1/2}, \quad (2)$$

(Bahcall & Peebles 1969) where $\Omega_{\rm m}$ is matter density and Ω_{Λ} is dark energy density parameter of the Universe. The quantity dn/dX also normalizes out the redshift dependence of the occurrence of the non-proximate absorbers along the line of sight. If dn/dX is flat, it indicates no comoving evolution meaning that the the product of absorber cross-section and comoving volume density is fixed for a population of absorbers.

We calculate the dn/dX following the steps outlined in section 6.3 of Davies et al. (2023a). For each ion, the intervening absorbers in the primary sample are binned into different redshift intervals in such a way that each redshift range covers similar path-lengths ($\Delta X = X(z_2) - X(z_1)$). The number of redshift bins for each ion is determined by ensuring that there is sufficient number of absorbers in each bin. The proximity limit used in this work is 10 000 km s^{-1} unless otherwise specified.

The survey completeness plays a major role in statistical analysis of the absorbers. Davies et al. (2023a) have characterized the completeness for the E-XQR-30 sample by creating 20 mock spectra for each quasar in the survey for which the absorber properties are known beforehand. These spectra are then processed in a similar way as the actual spectra to estimate the completeness as a function of the equivalent width, redshift, column density and b parameters for each of the ions. The sample completeness reaches 90 per cent at $W = 0.09$ Å and 50 per cent at $W = 0.03$ Å. For this study, we only retain absorbers with $W > 0.03$ Å and apply the completeness correction as a function of the equivalent width as follows:

$$\text{Completeness}(W) = S_y(\arctan(S_x W + T_x) + T_y), \quad (3)$$

where $S_x = 59.5$, $S_y = 0.39$, $T_x = -1.55$, and $T_y = 1.01$ (also see fig. 8 in Davies et al. 2023a).

To calculate the completeness-corrected dn/dX, the absorbers in each redshift interval are split into W bins of width 0.03 Å. For each W bin, the number of absorbers is divided by the completeness correction (equation 3) and these values are summed to get the total completeness-corrected number of absorbers in each redshift range. This method is applied to all absorbers studied in this work to correct for completeness unless otherwise specified, and rest-frame W values are used throughout. The completeness correction can also be applied to the absorbers as a function of column density (see fig. 8 and table 3 in Davies et al. 2023a); however, both methods give consistent results.

After obtaining the completeness corrected counts in each redshift bin, the absorption path-length interval, ΔX corresponding to each of those bins are calculated using the PYTHON code published with Davies et al. (2023a),[3] which removes masked regions from the absorption path.

Once the dn/dX values are calculated, the errors associated with dn/dX are computed using a Poisson distribution approximation for the absorber counts. The 1σ confidence limits of the dn/dX values are calculated using equations (9) and (14) from Gehrels (1986) for the upper and lower limits, respectively. The upper limit is calculated using

$$\lambda_u = (n+1)\left[1 - \frac{1}{9(n+1)} + \frac{S}{3\sqrt{n+1}}\right]^3. \quad (4)$$

The 1σ lower limit is estimated using

$$\lambda_l = n\left(1 - \frac{1}{9n} - \frac{S}{3\sqrt{n}} + \beta n^{\gamma}\right)^3, \quad (5)$$

where n is the number of absorbers. The parameter values of S, β, and γ are taken from table 3 of Gehrels (1986) corresponding to 1σ (0.8413) confidence limits. While calculating the errors, the completeness correction factor was also considered since dn/dX involves completeness corrected counts for each redshift interval. The dn/dX values are then plotted against path-length weighted mean redshift ($\langle z \rangle$) to see the cosmic evolution of the absorber.

3 RESULTS

The following sections show how the comoving line density dn/dX of each ion evolves with cosmic time and the effects of improved spectral resolution on the results compared with earlier works.

3.1 Mg II λ 2796Å and λ 2803Å

Mg II traces both neutral and ionized gas in metal-enriched galaxy haloes. Analysing the evolution of Mg II absorbers at high redshifts furthers our understanding of the mechanisms through which the haloes were populated with Mg II up to the peak of cosmic star formation at $z \approx 2$ (Matejek & Simcoe 2012). The E-XQR-30 metal absorber primary catalogue has 280 intervening Mg II systems among which 264 were detected with $W > 0.03$ Å in the redshift range 1.944–6.381 along a path-length of $\Delta X = 553.2$. Only systems with $W > 0.03$ Å are used to analyse their redshift evolution.

The Mg II absorbers are binned into five redshift intervals (see Table 1) in such a way that they cover similar absorption path-lengths with the exception of the highest redshift bin ($\Delta X = 17.76$). The redshift regions $3.81 < z < 4.05$ and $5.5 < z < 5.86$ are excluded because they correspond to contaminated wavelength regions where far fewer absorbers can be robustly measured. The dn/dX values

[2]The term 'comoving line density' in this work is same as 'number density', 'line density', and 'incidence rates' used in other publications.

[3]https://github.com/XQR-30/Metal-catalogue/tree/main/AbsorptionPathTool

Table 1. The dn/dX and Ω values of Mg II absorber systems using a proximity limit of 10 000 km s^{-1} after binning them in five redshift intervals. It can be seen that certain redshift intervals are masked. Counts are corrected for completeness using equation (3).

z range	$\langle z \rangle$	ΔX	Counts	Corrected counts	dn/dX	δ(dn/dX) (+,–)	$\Omega \times 10^{-8}$	$\delta\Omega \times 10^{-8}$
1.944–3.050	2.60	119.18	81	85.09	0.71	0.09, 0.08	14.39	8.33
3.050–3.810	3.44	118.73	68	69.63	0.59	0.08, 0.07	4.01	1.41
4.050–4.810	4.46	123.71	56	59.26	0.48	0.07, 0.06	2.39	1.13
4.810–5.500	5.15	123.18	50	51.97	0.42	0.07, 0.06	3.55	1.57
5.860–6.381	6.05	17.76	9	9.36	0.53	0.24, 0.17	0.26	0.12

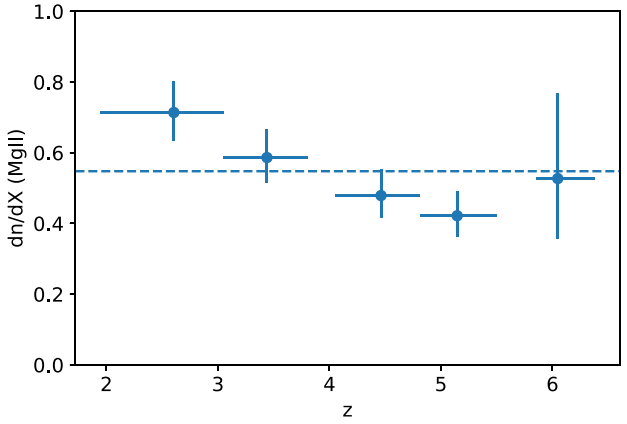

Figure 1. Evolution of the comoving line density of Mg II absorbers with redshift using a proximity limit of 10 000 km s^{-1}. The comoving line density of Mg II declines with redshift until $z \sim 5$ after which it is associated with larger errors. The normalized mean dn/dX value is denoted by a dashed horizontal line. For comparison with literature measurements at $z < 2$, see Fig. 3.

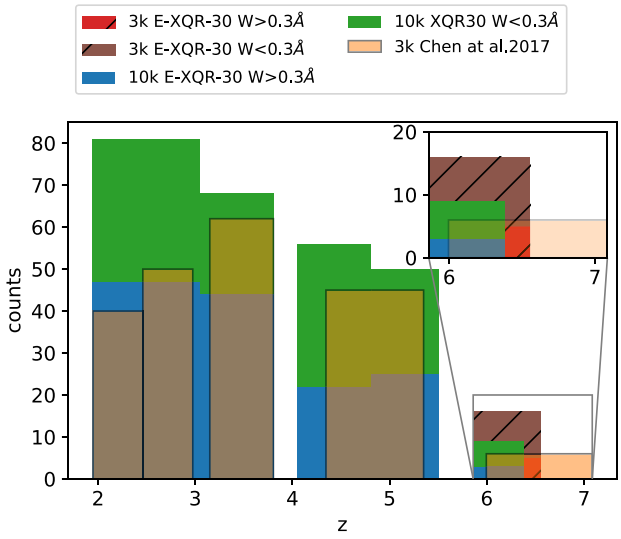

Figure 2. The number of intervening Mg II absorber systems in different redshift intervals from E-XQR-30 and C17. The E-XQR-30 sample is stacked on the basis of their rest-frame equivalent widths and only absorbers above 50 per cent completeness limit are shown here. The green bins show the weak absorbers, and the blue bins give the medium and strong absorber counts with a proximity limit of 10 000 km s^{-1}. As shown in the inset, the brown hatched bins give the new number of weak absorbers and the red hatched bins give the sum of medium and strong absorber counts when a smaller value of proximity limit (3000 km s^{-1}) is applied. It can be seen that when the proximity limit is reduced, it increases the width of the highest redshift bin and the number of $W < 0.3$ Å and $W > 0.3$ Å absorbers. The absorber counts from C17, which uses a proximity limit of 3000 km s^{-1}, are shown in a light orange colour. The medium and strong absorbers ($W > 0.3$ Å) from both works show a decline in the number counts with redshift while the weak absorbers ($W < 0.3$ Å) almost remain constant with redshift except for the highest redshift bin. The masked redshift regions for both E-XQR-30 and C17 are denoted by the gaps in the histogram.

obtained are shown in Table 1 and the trend in dn/dX across redshift z is shown in Fig. 1.

It is evident from Fig. 1 that Mg II absorbers decline in comoving line density with increasing redshift. A slight increase is seen at the highest redshift but it is associated with a large error due to few counts and small absorption path in the final bin. Therefore, the increase from $\langle z \rangle \sim 5$ to $\langle z \rangle \sim 6$ is not statistically significant given the errors.

It is also interesting to see how the Mg II absorbers evolve with redshift if they are sub-divided based on their strength. Previous studies of strong Mg II absorbers indicate that they trace global SFH through galactic outflows and weak Mg II systems trace the accreting and co-rotating gas in galaxy haloes (see Sections 4.1 and 4.2). Chen et al. (2017, hereafter C17) is a large survey of high-redshift Mg II absorbers using 100 quasars at $3.55 \leq z \leq 7.09$ with the Magellan/FIRE spectrometer detecting 280 Mg II absorbers. C17 analysed the evolution of medium and strong Mg II absorbers by applying a proximity limit of 3000 km s^{-1}.

E-XQR-30 has detected 66 out of 70 Mg II absorber systems from the 19 quasars that were used in C17 because one of the missing systems falls in a noisy region and the other three systems were observed to be better explained by other ion transitions at various redshifts. In addition, the survey enabled the detection of 95 additional systems in those quasars due to the improved sensitivity (Davies et al. 2023a). A histogram of the number counts of the intervening Mg II absorbers with different strengths used for the dn/dX analysis between this work and C17 across different redshift intervals is shown in Fig. 2. The E-XQR-30 sample is divided into two groups; one group consisting of only weak absorbers ($W < 0.3$ Å) and the other group with both medium and strong absorbers ($W > 0.3$ Å) for better comparison with C17. Although C17 were able to detect some weak systems, the overall completeness of their data was not enough to produce robust statistical data. We present for the first time a large population of weak intervening Mg II (123 absorbers after applying the 50 per cent completeness cut and masking the contaminated redshift intervals) at $2 < z < 6$ sufficient for a statistical analysis. For E-XQR-30, the weak absorbers are stacked on top of the absorbers with $W > 0.3$ Å shown in green and blue bins, respectively. The number of absorbers from C17 is shown in light orange. It is evident from the histogram that E-XQR-30 has a larger total sample available for analysis after applying the completeness limit and a larger proximity limit of 10 000 km s^{-1}. However, C17 has a slightly

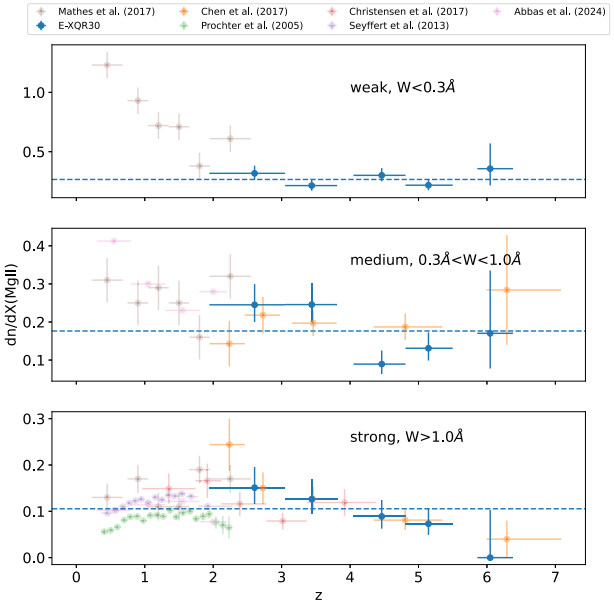

Figure 3. Redshift evolution of Mg II absorbers divided into three samples according to their equivalent widths and using 10 000 km s^{-1} as the proximity limit. The results from E-XQR-30 are shown in blue and those from C17 are given in orange. The dn/dX values at lower redshift from various literature are also included in the figure. The top panel shows the evolution of weak Mg II absorbers (W < 0.3 Å). The middle and bottom panels show the evolution of medium and strong Mg II absorbers, on which the dn/dX values from C17 are also plotted. The blue-dashed horizontal lines in each panel represent the path-length weighed mean dn/dX for E-XQR-30 sample. The dn/dX of absorbers with W < 1.0 Å show a flat evolution with redshift for z > 2 while those with $W \geq$ 1.0 Å show a decline in comoving line density towards z > 2.

bigger sample if only absorbers with W > 0.3 Å (medium and strong) absorbers are considered due to their larger number of background quasars. The histogram shows a wider bin at the highest redshift interval for C17 compared to the E-XQR-30 bin because the former observed quasars that covered broader redshift ranges. The effect of using a smaller proximity limit on the sample size and the total redshift range covered is also investigated in this work. When the proximity limit for E-XQR-30 is changed to 3000 km s^{-1}, the upper limit of the redshift bin changes from 6.381 to 6.555 and the number of absorbers in the last redshift bin increases slightly, as shown by the hatched brown and red-coloured bins in the inset. There is a total increase of seven absorbers: five weak and two medium. It should also be noted that the number of strong absorbers remained zero even after reducing the proximity limit.

Fig.3 shows the evolution of the Mg II comoving line density with redshift for different strengths of the absorbers. The absorbers are subdivided based on their equivalent widths: W < 0.3 Å, 0.3 < W < 1.0 Å and W > 1.0 Å. The dn/dX values for Mg II absorbers with different equivalent widths and redshifts can be found in Table 2. There are three interesting findings worthy of further discussion: the remarkably high dn/dX, the flat evolution of weak and medium (W < 1.0 Å) systems with redshift at 2 < z < 5, and the potential upturn at z > 5.

As demonstrated in Codoreanu et al. (2017) and C17, associating each Mg II absorber with a single galaxy [at a limiting magnitude ($M_{\rm AB} \leq -17.5$) or halo mass cut (log $M_{\rm h}$ > 10.2), respectively] cannot reproduce the high-redshift dn/dX to within a factor of 10 or more. Both studies adopt observationally derived scaling relations in which the CGM absorption radius scales with halo mass and the covering fraction for weak Mg II absorbers is greater than 80 per cent within 50 kpc (Churchill et al. 2013; Nielsen, Churchill & Kacprzak 2013). The superior spectral resolution and higher S/N of our study that includes weak Mg II systems further underscores the tension since dn/dX is dominated by weak systems (see y-axis of Fig. 3). C17 were able to reconcile the tension, at least with medium absorbers, by allowing the mass cut to vary with redshift, and further integrating down the galaxy mass function as z approaches six to include galaxies with log $M_{\rm h}$ > 8 (=log M_* > 7).

The comoving line density of strong absorbers (W > 1.0 Å) show a declining trend with redshift. Thus, the decrease in dn/dX for the total sample (see Fig. 1) can be attributed to this decline to $z \sim 5$, while the upturn (with high error bars) at the highest redshift bin could be due to the increase at $\langle z \rangle \sim 6$ in comoving line density of absorbers with W < 0.3 Å. This upturn is not statistically significant due to the short path-length of this redshift bin. More observations focusing on redshifts z > 5 must be made to reach robust conclusions.

The dn/dX evolution of Mg II using the E-XQR-30 metal absorber catalogue agrees with the results of C17 for medium and strong absorbers (W > 0.3 Å), although there are differences in the path-length weighted mean redshifts at which the dn/dX values are calculated. The difference in the proximity limits used in both works must also be taken into consideration when comparing the results. Adopting a 3000 km s^{-1} proximity limit to match C17 analysis results in dn/dX values similar to the 10 000 km s^{-1} (see Table 2). Therefore, we chose to plot the primary E-XQR-30 catalogue values in Fig. 2. The consistency in the comoving line density statistics regardless of the proximity limits used, shows that our measurements are robust to the choice of proximity zone limit.

This work is also consistent with the results from other Mg II comoving line density analyses such as Matejek & Simcoe (2012), Codoreanu et al. (2017), and Zou et al. (2021). The work of Matejek & Simcoe (2012) is a precursor of C17 using 46 quasar spectra from FIRE. They observed no evolution for absorbers with 0.3 < W < 1.0 Å while the dn/dX of strong absorbers in their work showed a slight increase until $z \sim 3$, which could be due to the small number of detections in the corresponding redshift intervals, after which they decline with redshift. Codoreanu et al. (2017) detected 52 Mg II absorbers in the redshift range 2 < z < 6 from high-quality spectra of four high-z quasars from XSHOOTER where they demonstrated a flat redshift evolution of dn/dX for weak and medium absorbers although the evolution of strong absorbers was subjected to limited sample size. Also, Zou et al. (2021) obtained the dn/dX values of strong Mg II absorbers at 2.2 < z < 6.0 using Gemini GNIRS which are consistent with the E-XQR-30 results. Furthermore, our remarkably flat dn/dX for weak Mg II absorbers provides context for the anticipated cross-correlation analysis of the Mg II forest from *James Webb Space Telescope* (*JWST*) data (Hennawi et al. 2021).

In Fig. 3, dn/dX values from Mg II absorber surveys at lower redshift are also included to compare the absorber evolution at z < 2 with the results from our work. Prochter et al. (2006) studied strong Mg II absorbers across 0.35 < z < 2.3 and found that they roughly follow the global star formation rate density. Similar findings have been reported by Seyffert et al. (2013) on strong Mg II which are found to increase by 45 per cent approximately from z = 0.4 to 1.5 associating these systems with outflows from star-forming galaxies. The dn/dX from Christensen et al. (2017) for strong systems at 0.9 < z < 4.4 roughly agrees with the trends in previous high-resolution surveys including our work peaking at $\langle z \rangle \sim 1.9$ and then declining towards high redshift. Mathes et al. (2017) studied the evolution of Mg II with equivalent widths W > 0.01 Å

Table 2. The dn/dX values for Mg II absorbers based on the strength of the absorption profiles. A proximity limit of 10 000 km s^{-1} is used here and the grey-shaded regions show the dn/dX of Mg II absorbers for a proximity limit of 3000 km s^{-1} for comparison with C17. There is no significant change when the proximity limit is changed. The completeness of the sample is equal to unity at $W > 1.0$ Å.

z range	$\langle z \rangle$	ΔX	Counts	Corrected counts	dn/dX	δ(dn/dX) (+, −)
			$W_{\rm Mg\,II} < 0.3$ Å			
1.944–3.050	2.60	119.18	34	37.88	0.32	0.06, 0.05
3.050–3.810	3.44	118.72	24	25.46	0.21	0.05, 0.04
4.050–4.810	4.46	123.71	34	37.20	0.30	0.06, 0.05
4.810–5.500	5.15	123.18	25	26.83	0.22	0.05, 0.04
5.860–6.381	6.05	17.76	6	6.34	0.36	0.21, 0.14
5.860–6.555	6.06	35.87	11	11.73	0.33	0.13, 0.09
			$0.3 < W_{\rm Mg\,II} < 1.0$ Å			
1.944–3.050	2.60	119.18	29	29.21	0.25	0.05, 0.05
3.050–3.810	3.44	118.73	29	29.17	0.25	0.05, 0.05
4.050–4.810	4.46	123.71	11	11.05	0.09	0.04, 0.03
4.810–5.500	5.15	123.18	16	16.14	0.13	0.04, 0.03
5.860–6.381	6.05	17.76	3	3.02	0.17	0.17, 0.09
5.860–6.555	6.06	35.87	5	5.04	0.14	0.09, 0.06
			$W_{\rm Mg\,II} > 1.0$ Å			
1.944–3.050	2.60	119.18	18	18	0.15	0.045, 0.04
3.050–3.810	3.44	118.73	15	15	0.13	0.04, 0.03
4.050–4.810	4.46	123.71	11	11	0.09	0.04, 0.03
4.810–5.500	5.15	123.18	9	9	0.07	0.03, 0.02
5.860–6.381	6.05	17.76	0	0	0	0.10, 0
5.860–6.555	6.06	35.87	0	0	0	0.05, 0

at $0.1 < z < 2.6$ and thereby calculated the dn/dX of weak, medium and strong absorbers. Recently, Abbas et al. (2024) analysed the evolution of Mg II absorbers with $W > 0.3$ Å using a new method to measure the column densities of Mg II systems using the Australian Dark Energy Survey (OzDES) over the redshift range of $0.33 \leq z \leq 2.19$. The dn/dX values from the above-mentioned earlier works are colour coded accordingly as given in the legend at the top of the figure. At $z < 2$, the weak systems are observed to increase towards the present epoch which can be attributed to the metallicity build-up and the decreasing intensity of the ionizing radiation in the CGM giving rise to more weak absorbers. The constant evolution of medium Mg II absorbers at $z > 2$ extends to lower redshifts in such a way that the number density of the absorbers balances out the absorber cross-section across the whole redshift range. However, strong Mg II absorber evolution, in general, traces the trend in global SFH (Madau & Dickinson 2014) which rises across cosmic time until $z \sim 2$ after which it shows a gradual decline towards the present epoch.

Using a single sightline from deep XSHOOTER survey, Bosman et al. (2017) detected five intervening Mg II systems at $z > 5.5$ with three of them being weak absorbers showing that there is a possibility of steepening of equivalent width distribution at low equivalent widths. This is in agreement with the large number of detections of Mg II with $W < 0.3$ Å at $z > 2$ in this work. Using the weak absorbers sample, the prediction by Bosman et al. (2017) can be verified by plotting the equivalent width distribution given by

$$\frac{{\rm d}^2 n}{{\rm d}z{\rm d}W} = \frac{N}{\Delta W \Delta z}, \tag{6}$$

where ΔW is the equivalent width range and Δz is the redshift path-length. The blue points in Fig. 4 indicate the W distribution for the total sample of Mg II that are completeness corrected.

Nestor, Turnshek & Rao (2005) have shown that equivalent width distribution for Mg II absorbers with $W > 0.3$ Å can be fitted by an exponential function given by

$$\frac{{\rm d}^2 n}{{\rm d}z{\rm d}W} = \frac{N^*}{W^*} {\rm e}^{-W/W^*}, \tag{7}$$

where N^* is the normalization factor and W^* determines the exponential curve growth or decay. But Bosman et al. (2017) showed that a single exponential function might not be the best fit over the whole range of equivalent width. We fit the W distribution for the Mg II absorbers from this work at $1.9 < z < 6.4$ using equation (7) and the fit is indicated by the dashed orange curve in Fig. 4. The best-fitting parameter values obtained are $W^* = 0.47 \pm 0.04$ and $N^* = 1.95 \pm 0.36$.The function is a good fit for low equivalent widths but not for $W > 1.0$Å proving the prediction of Bosman et al. (2017). As a result, we then fit the distribution using a Schechter function of

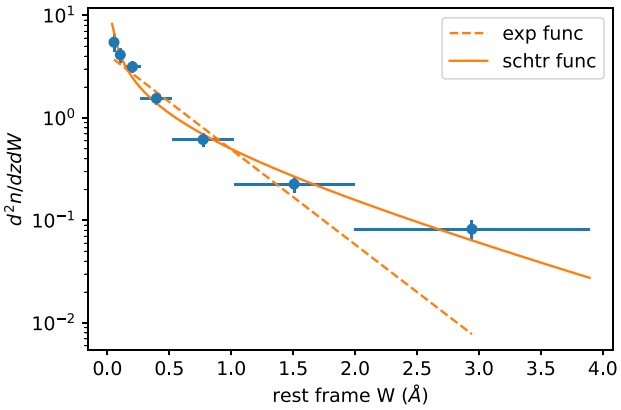

Figure 4. Mg II equivalent width distribution for the total sample corrected for completeness. The exponential function fit is shown in dashed orange and the Schechter function is shown in solid orange, which is a better fit for the equivalent width distribution.

Table 3. The dn/dX values of C II with the associated errors at different redshift intervals adopting a proximity limit of 10 000 km s^{-1}.

z range	$\langle z \rangle$	ΔX	Counts	Corrected counts	dn/dX	δ(dn/dX) (+,–)
5.169–5.679	5.51	38.88	6	6.77	0.17	0.10, 0.07
5.679–6.381	5.89	38.90	13	14.09	0.36	0.13, 0.09

the form

$$\frac{\mathrm{d}^2 n}{\mathrm{d}z\mathrm{d}W} = \left(\frac{\Phi^*}{W^*}\right)\left(\frac{W}{W^*}\right)^{\alpha} \mathrm{e}^{-W/W^*}, \quad (8)$$

following the approach of Kacprzak & Churchill (2011); Mathes et al. (2017) at $z < 2$ and Bosman et al. (2017) at $z > 6$. Here, Φ^* is the normalization factor, α is the low equivalent width power slope and W^* is the turn over point where the low equivalent width power-law slope shifts to an exponential cut-off. Using chi-square statistic, the best-fitting parameters are estimated to be $W^* = 1.44^{+0.32}_{-0.26}$ Å, $\Phi^* = 1.13^{+0.16}_{-0.15}$ and $\alpha = -0.66^{+0.09}_{-0.07}$. However, these values are different from those computed by Bosman et al. (2017) for their sample of 3 absorbers at $5.9 < z < 7$. The fit using the Schechter function is represented in solid orange in Fig. 4, and provides a better fit than the exponential function. The redshift evolution of the equivalent width distribution is also explored in this work and the slope of the distribution is observed to steepen with redshift. More details can be found in Appendix A.

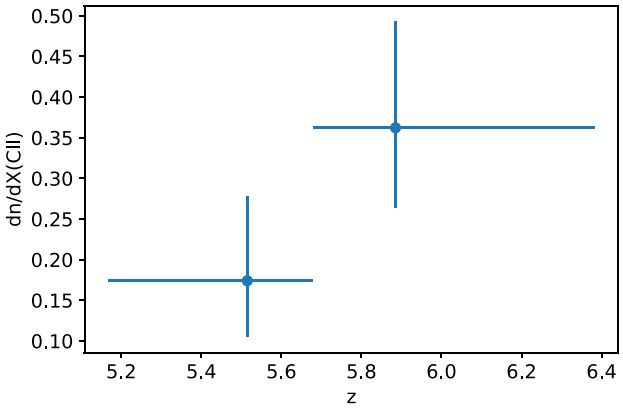

Figure 5. The evolution of C II absorbers across redshift applying a proximity limit of 10 000 km s^{-1}. The absorbers have $W > 0.03$ Å. An increasing trend of comoving line density can be seen in the figure.

3.2 C II λ1334Å

C II is one of the abundant ions present in the galaxy haloes tracing the metal-enriched gas, where hydrogen is largely neutral. Since the first ionization energy of carbon (11.26 eV) is less than 13.6 eV, it will appear as singly ionized carbon (C II) in the otherwise neutral medium (Becker et al. 2015a).

The primary E-XQR-30 absorber catalogue contains 22 intervening C II absorbers observed along a path-length of $\Delta X = 77.8$ in the redshift interval $5.169 < z < 6.381$. Since there is only one strong C II transition in the searched spectral window, it is important to look for other low-ionization transitions associated with C II such as O I λ1302Å, Si II λλ1260Å, 1526Å or Al II λ1670Å to confirm the identification. The C II candidates are rejected if the probed spectral region reveals a non-detection of Si II and O I because these associated ions are expected to have comparable equivalent widths (Becker et al. 2019; Davies et al. 2023a).

The comoving line density evolution of C II is calculated using the same method applied to Mg II. Only 19 C II systems with $W > 0.03$ Å are considered. Due to the short path-length available for C II detection redward of the saturated Lyman-α forest, we split the available redshift range into two bins with equal path-lengths, ΔX. The redshift ranges, dn/dX and the associated errors are given in Table 3. The evolution of C II absorbers with redshift is shown in Fig. 5. The dn/dX value for C II doubles from $\langle z \rangle = 5.5$ to 5.9.

Cooper et al. (2019, hereafter C19) compared column densities of low- and high-ionization carbon (C II/C IV) at $z > 5$ using the spectra of 47 quasars from Magellan/FIRE and Keck/HIRES. C19 found that at $z > 5.7$, high-ionization absorbers are very weak or undetected relative to LIAs.

The E-XQR-30 has a higher spectral resolution when compared with C19 (except for the one quasar from Keck/HIRES) and thus, it is worthwhile comparing how the improved data quality has affected the overall trend in C II evolution. There are 11 common quasar lines of sight with the E-XQR-30 sample and all systems reported in C19 were recovered and 11 additional systems were also detected (Davies et al. 2023a). Using 48 quasar spectra, C19 detected 35 C II systems (16 among them are limits) at $z > 5$ compared to the 46 C II (both proximate and non-proximate) detections in E-XQR-30. C19 found that the highest redshift absorbers are more likely to be detected only in C II or Mg II. This has been further confirmed through the works of D'Odorico et al. (2010, 2013) where the C IV comoving line density and/or cosmic mass density decline with increasing redshift. The decrease in the densities of highly ionized carbon towards lower redshifts is also supported by the findings of Becker et al. (2019) where they observe a decline in the equivalent width ratios of C IV to O I (detected in association with C II absorption lines) with redshift. Furthermore, Davies et al. (2023b) (see fig. 7 in their paper) has illustrated the relative contributions of C II and C IV to the cosmic mass density evolution of carbon, where $\Omega_{\mathrm{C\,IV}}$ declines with redshift and $\Omega_{\mathrm{C\,II}}$ increases across $5.2 < z < 6.4$.

Other works on high-redshift chemical enrichment such as Becker et al. (2011) and Bosman et al. (2017), using their very small samples, found that the comoving line density evolution of LIAs such as C II at $5 < z < 7$ is similar to that of low-ionization systems traced by damped Lyman alpha (DLA – $\log N_{\mathrm{H\,I}}/\mathrm{cm}^2 \geq 20.3$) and sub-DLA ($19.0 < \log N_{\mathrm{H\,I}}/\mathrm{cm}^2 < 20.3$) systems across $3 < z < 5$, tentatively suggesting a constant evolution. Conversely, the dn/dX calculated using the relatively larger sample with higher S/N data from E-XQR-30 show that the C II absorbers increase in density at higher redshifts. Also, cosmological hydrodynamic simulations such as Finlator et al. (2015) and Keating et al. (2016) predicted a slow decrease in C II number density per absorption path contrary to the observed upturn for C II in this work. Considerable work has to be done in modelling the chemical enrichment of early Universe to match the observations. Furthermore, high-resolution cosmological simulations on chemical enrichment of early Universe like Oppenheimer et al. (2009) show that C II absorbers trace low-mass galaxies at higher redshifts which are believed to be the major contributors of ionizing flux during EoR (Robertson et al. 2013; Duffy et al. 2014; Wise et al. 2014; Finkelstein et al. 2019; Matthee et al. 2022; Yeh et al. 2022).

Table 4. The dn/dX values of O I using different proximity limits. The proximity limits, redshift ranges, path-length weighted mean redshift, absorption path-length, raw counts, and completeness corrected counts, associated errors with dn/dX are also given in the table.

Proximity (km s^{-1})	z range	$\langle z \rangle$	ΔX	Counts	Corrected counts	dn/dX	δ(dn/dX) (+,–)
10000	5.322–5.742	5.60	23.17	3	3.83	0.17	0.16, 0.09
10000	5.742–6.381	5.96	23.19	5	5.61	0.24	0.16,0.10
5000	5.322–5.813	5.65	34.51	5	5.89	0.17	0.12, 0.07
5000	5.813–6.505	6.03	34.53	10	11.26	0.33	0.14, 0.10

3.3 O I λ1302Å

O I absorption line traces the neutral gas in the galaxy haloes because its first ionization potential is very close to hydrogen and due to charge exchange $n(O^+)/n(O) \approx n(H^+)/n(H)$ over a wide variety of physical conditions (Chambaud et al. 1980; Osterbrock & Ferland 2006; Becker et al. 2015a, 2019). The E-XQR-30 detects 29 O I systems out of which 10 are intervening absorbers (10 000 km s^{-1} proximity limit) in the primary sample across a redshift range of $5.3 < z < 6.4$ covering a path-length of $\Delta X = 46.359$. All O I detections in the catalogue have associated C II transitions (Davies et al. 2023a).

As outlined in Section 2.2, the absorbers are binned into two redshift bins covering equal ΔX. After applying the 50 per cent completeness limit, the number of systems reduces to 8. The absorber counts in each redshift bin are completeness corrected and the resultant dn/dX values are given in Table 4.

Becker et al. (2019, hereafter B19) detected 57 intervening O I systems using 199 quasar spectra from Keck/ESI and VLT/XSHOOTER across $3.2 < z < 6.5$ with an S/N ratio of 10 per 30 km s^{-1} at a rest wavelength of 1285 Å. These absorbers are separated from the quasar emission redshift by a velocity separation of >5000 km s^{-1}. B19 reported a rapid increase in the comoving line density of O I at $5.7 < z < 6.5$ covering a path-length of $\Delta X = 66.3$. This is $2.5^{+1.6}_{-0.8}$ times greater than the comoving line density across $4.9 < z < 5.7$.

A scatter plot along with histograms that compare the distribution of intervening O I absorbers along redshift and equivalent width between E-XQR-30 and B19 is shown in Fig. 6. The blue colour represents the data from E-XQR-30 using the proximity limit adopted in the catalogue. The O I systems from B19 that use 5000 km s^{-1}as proximity limit are coloured orange. The errors in equivalent width are also shown in the scatter plot. The histogram on top shows the redshift distribution of both data sets. The E-XQR-30 has data only in the high-redshift range, as the survey focuses only on quasars at $z >$ 5.8. The histogram on the right gives the equivalent width distribution of O I data from both surveys. The E-XQR-30 data consist of O I absorbers with $W \lesssim 0.4$ Å where most of the absorber population from B19 lie in the scatter plot. However, the equivalent widths of data from B19 range between $0.02 < W < 0.9$ Å.

To compare with B19, the additional absorbers obtained by switching to a 5000 km s^{-1} proximity limit are shown in green in the scatter plot and histograms. The number of intervening absorbers increased from 10 to 17 and the absorption path-length increased to $\Delta X = 69.038$. Adopting the new proximity limit also improved the consistency of the dn/dX results with B19.

Fig. 7 depicts the redshift evolution of comoving line density of O I absorbers from E-XQR-30 with different proximity limits together with the results from B19. The dark blue points are the dn/dX for data from E-XQR-30 using a proximity limit of 10 000 km s^{-1}and the light blue squares are those with a proximity limit of 5000 km s^{-1}. The results from the work of B19 is shown in orange dots. It is interesting to observe the upturn at $z \gtrsim 5.7$ even with the small number of O I absorbers from our survey. Cosmic variance may offer an explanation to the minor discrepancies in the dn/dX values between our work and B19. However, the values agree with B19 within the 1σ error bars.

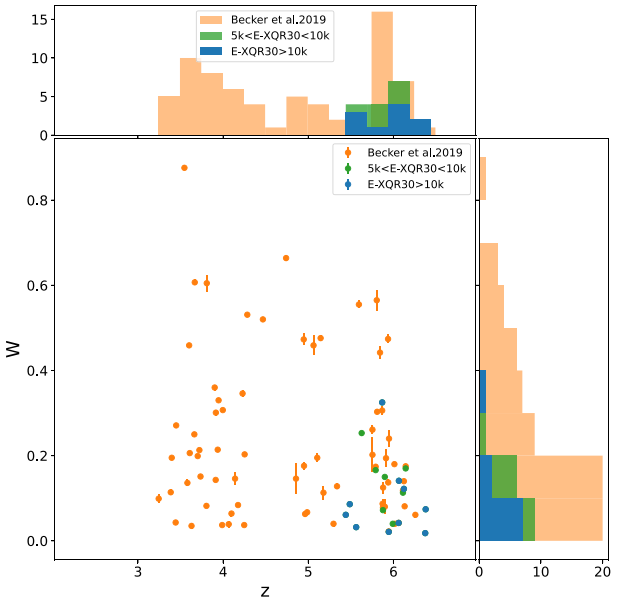

Figure 6. A scatter plot with histograms showing the sample distribution of B19 and E-XQR-30 intervening O I absorbers. The blue-coloured scatter points represent E-XQR-30 data with a proximity limit of 10000 km s^{-1} while the green-coloured points show the E-XQR-30 O I absorbers lying between 5000 and 10000 km s^{-1}. The orange dots represent the B19 data which uses a proximity limit of 5000 km s^{-1}. The top histogram gives the redshift distribution for O I data sets from B19 and E-XQR-30 with different proximity limits. Similarly, the histogram on the right gives the rest-frame equivalent width distribution of the data in the scatter plot. The figure demonstrates that the E-XQR-30 sample consists of O I absorbers with $W < 0.4$ Å at $z > 5.3$ compared to the B19 sample.

Only 21 quasars in their sample are included in our survey and Davies et al. (2023a) have successfully recovered all O I systems reported in B19 along with the detection of one additional system. Sondini et. al. (in preparation) analyse the E-XQR-30 data and report two additional O I absorbers that fall strictly outside the Lyman α forest cutoff adopted by the Davies et al. (2023a) catalogue: PSO J060+24 at $z = 5.6993$ and SDSSJ0100+2802 at $z = 5.7974$. There is also a chance of clustering of O I absorbers at high redshift $z \sim 6$ as reported in B19 due to the fluctuations in UV background towards

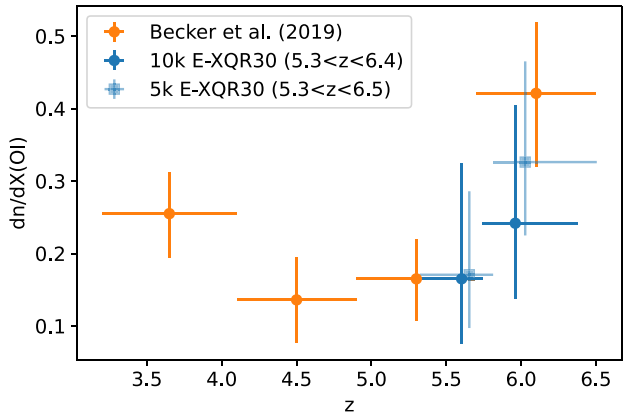

Figure 7. The comoving line density of O I using E-XQR-30 in comparison to the work of B19. Only O I absorbers with $W > 0.03$ Å are used in the analysis. The dark blue circles show the dn/dX calculated for O I across $5.3 < z < 6.4$ by applying a proximity limit of 10000 km s^{-1} while the light blue squares are the dn/dX values for O I across $5.3 < z < 6.5$ using a proximity range of 5000 km s^{-1} from E-XQR-30. The orange points show the dn/dX values in B19 which used 5000 km s^{-1} as the proximity limit. The figure shows an upturn in the comoving line density of O I at $z > 5.3$ which is consistent with B19 results.

the tail end of EoR (e.g. D'Aloisio et al. 2018; Kulkarni et al. 2019). Completeness variations are explored in Appendix B.

3.4 Comparison with *JWST*/NIRSpec results on metal enrichment

Recently, Christensen et al. (2023) observed four quasar sightlines at $z > 6.5$ using NIRSpec on *JWST* and studied the evolution of metal enrichment at $2.42 < z < 7.48$. Their quasar spectra cover a wider spectral range and have high S/N of 50–200 but with lower spectral resolution of $R \simeq 2700$ compared with E-XQR-30. Using the four quasar spectra, they detected 61 systems at $2.42 < z < 7.48$ and calculated the comoving line density of these systems including the ions that we studied in this work. The one quasar common in both works is J0439+1634 at $z = 6.52$. Davies et al. (2023a) detected 43 absorption systems from the spectrum, while Christensen et al. (2023) detected only 17 systems including an additional Mg II doublet at $z = 6.208$. The non-detected systems include several weak Mg II absorbers, weak C IV doublets and Si IV doublets at $2.3 < z < 5.3$ (Christensen et al. 2023) emphasizing the critical need for median resolution spectroscopy in the *JWST*-era.

The proximity limit adopted by Christensen et al. (2023) is 3000 km s^{-1}, although J0439+1634 is affected by BAL regions to larger velocities of ∼10 000 km s^{-1}. They examined the redshift evolution of LIAs using 6 O I (two of them are new detections at $z > 7$), 8 C II intervening systems at $6.4 < z < 7.4$ and observed an upturn for O I and C II at $z > 6$. They also studied the evolution of 48 Mg II (one of them is a new detection at $z \sim 7.443$) intervening systems with $W > 0.3$ Å at $2.4 < z < 7.45$ and observed a constant evolution for Mg II. However, dn/dX values across redshift in our work using a large sample of Mg II show that they decline with redshift at least until $z \sim 5$. Their work also illustrates a decline in strong Mg II comoving line density evolution. Overall, the results from *JWST*/NIRSpec are consistent with the results from this work for O I, C II, and strong Mg II.

4 DISCUSSION

4.1 The nature of weak Mg II absorbers at high redshift

This work presents for the first time a significant population of 131 intervening weak Mg II absorbers sufficient to produce robust statistical results in their evolution. There are several low-redshift ($z < 2$) studies in the literature finding that weak absorbers are distributed along the major axis of face on, blue galaxies (Kacprzak et al. 2012; Nielsen et al. 2015) tracing the infalling gas into the CGM and they have little correlation between the absorber equivalent width and the galaxy colour (Chen et al. 2010; Kacprzak et al. 2011). Furthermore, Churchill et al. (2005) and Chen et al. (2010) have showed that weak Mg II absorbers do not necessarily trace low surface brightness galaxies by studying galaxy absorber pairs at intermediate and low redshifts, respectively. Recent high-redshift metal absorber surveys reported detections of weak Mg II absorbers, however, there were not enough sightlines or sensitivity to produce a large population of weak absorbers sufficient to measure their cosmic evolution. For example, C17 reported 59 detections of weak Mg II absorbers, however, their overall completeness was not enough to produce robust statistics on them. Similarly, works by Codoreanu et al. (2017) and Bosman et al. (2017) also presented weak Mg II detections, but they were also limited in their sample size (10 systems at $2 < z < 5$ and 3 systems at $z > 5.5$, respectively).

In this work, weak Mg II absorbers account for 47 per cent of the total completeness corrected number of intervening Mg II absorbers in E-XQR-30. It has been observed that the evolution of weak Mg II absorbers remain constant – within a factor of 2 – in a redshift range of $1.9 < z < 6.4$ from Fig. 3.

Much literature exists on the association of weak Mg II systems and the relative number density of LLSs, the role of SFR and metallicity trends, dwarf galaxies and the UVB at $z < 2$. With the benefit of a long lever arm from $z = 1.9$ to 6.4, these hypotheses can be tested. At lower redshifts, $0.4 \leq z \leq 1.4$, it is assumed that the weak Mg II absorbers arise in the sub-LLS environments because the weak absorbers outnumber the LLS absorbers in comoving line density (Churchill et al. 1999). Crighton et al. (2019), using a data set of 153 optical quasar spectra from the Giant Gemini GMOS survey ($3.5 < z < 5.4$) and complementary literature data to calculate the incidence of LLS absorbers per unit absorption path-length (dn/dX), which increases steeply from redshift 0 through to 5.4. Since the dn/dX of weak Mg II absorbers is flat, swapping from being more numerous than LLSs at $z < 2$ to three times rarer at $z > 4$, is only possible if the covering fraction varies by the same amount. Dutta et al. (2020) find that the covering fraction of weak Mg II systems does not change from low redshift out to $z \sim 1.5$. Nevertheless, due to the metallicity and the ionization effects at high z, the neutral hydrogen column density of systems detected as weak Mg II increases and consequently, LLSs could be associated with weak Mg II absorbers (Steidel & Sargent 1992; Churchill et al. 1999; Rigby et al. 2002). Our results support this picture with a factor of 3 drop in the covering fraction out to redshift ∼6.

Along the same lines, we can now examine the association of weak Mg II absorbers at $0 < z < 2.4$ and the SFH of dwarf galaxies (Churchill et al. 1999; Lynch, Charlton & Kim 2006; Lynch & Charlton 2007; Narayanan et al. 2008), which both peak at $z \sim 1$ and drop at $z \sim 2$. Knowing that dn/dX continues at a constant level to $z \sim 6$, indicates this hypothesis cannot continue to high redshift. As mentioned in Section 3.1, C17 were able to reconcile the Mg II dn/dX evolution to $z \sim 6$ by allowing the associated galaxy mass to decrease with increasing redshift. Whatever the mechanisms

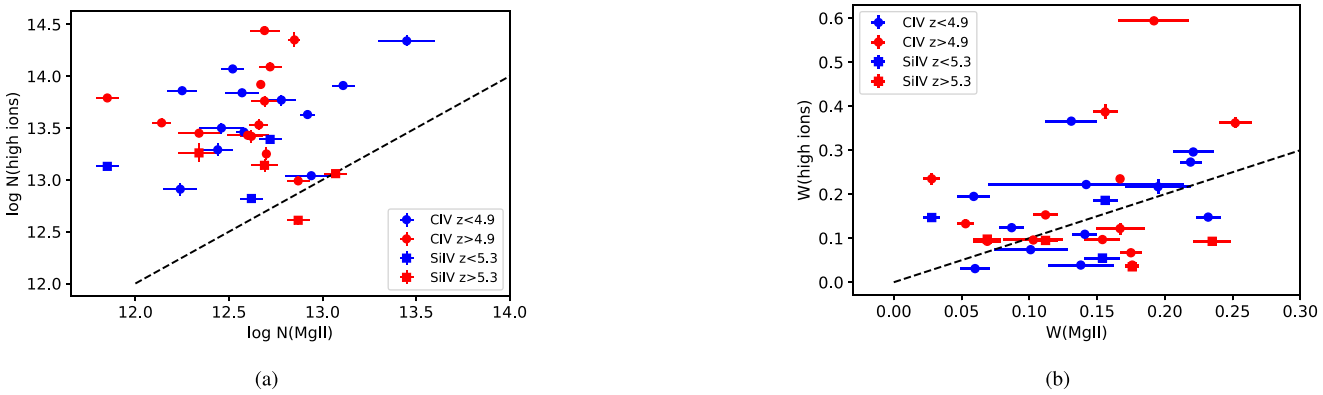

(a) (b)

Figure 8. The left panel shows the column densities of high-ionization absorbers, C IV and Si IV versus the column densities of weak Mg II absorbers. The right panel shows the rest-frame equivalent widths of the C IV and Si IV absorbers against the equivalent widths of weak Mg II absorbers. Both the associated C IV and Si IV are divided based on the median value of the redshift for the sample. The dots represent the C IV sample; blue indicates the lower redshift and red indicates the higher redshift samples. The squares stand for the Si IV sample; blue showing the lower redshift and red showing the high-redshift sample. The dashed line represents the 1:1 relation between the respective parameters of the high-ionization absorbers and weak Mg II. The figure depicts that weak Mg II systems have higher column densities of C IV and Si IV and both weak Mg II and high-ionization absorbers have comparable equivalent widths.

that give rise to weak Mg II, it should be able to replenish them in such a way that the comoving line density of these low equivalent width absorbers do not change considerably across cosmic time.

The weak Mg II absorbers are also associated with high-ionization absorbers such as C IV and Si IV indicating a multi-ionization phase for these weak absorbers. Among 58 intervening weak Mg II absorbers from primary sample across the redshift range where C IV and Si IV can be detected, 25 of them are associated with C IV at $4.3 \leq z \leq 6.3$ and 7 of them are associated with Si IV at $4.9 \leq z \leq 6.3$. We have not used the 50 per cent completeness cut here to find out the fraction of Mg II absorbers with high ionization species. This constitutes 43 per cent of weak Mg II absorbers with C IV across $\Delta X = 211.8$ and 25 per cent of weak Mg II with Si IV across $\Delta X = 120.6$. Among the weak Mg II absorbers associated with high-ionization absorbers, six of them have both C IV and Si IV detections. Most of these weak Mg II absorbers are single-component systems at the resolution of XSHOOTER. Both the C IV and the Si IV absorbers are detected in weak Mg II systems up to a redshift of $z \sim 5.9$ after which no C IV or Si IV associations are found. This might be because of the decrease in high-ionization absorber comoving line density (C19; D'Odorico et al. 2022; Davies et al. 2023b) at higher redshifts due to lower metal abundance and a softer ionizing background (Finlator et al. 2016; C19). We also examined whether the absence of weak Mg II systems with C IV and Si IV at $z > 5.9$ is due to the lower S/N of the quasar spectra towards these redshifts and found that the typical S/N of the spectra is roughly equivalent at both $4.3 < z < 5.9$ and $5.9 < z < 6.3$. The relation between the column densities of the high-ionization absorbers, C IV and Si IV, against the column densities of weak Mg II absorbers is shown in Fig. 8(a). Similarly, the equivalent widths of C IV and Si IV are plotted against the equivalent widths of weak Mg II in Fig. 8(b). In both figures, the dots represent C IV detections associated with weak Mg II and the squares represent Si IV associated with weak Mg II. Both the samples are divided based on their median redshift and the low-redshift sample is depicted using blue colour and the high-z sample is shown using red colour. A dashed line representing the 1:1 relation between the column densities (equivalent widths) of high-ionization absorbers and the weak Mg II absorbers is marked on both the figures. It can be observed from the left panel in Fig. 8 that half of the weak Mg II absorbers in the E-XQR-30 sample are rich in triply ionized carbon and silicon because most of the points lie on the upper region of the 1:1 line. The right panel in Fig. 8 shows that the strengths of the absorbers are comparable between the high-ionization absorbers and weak Mg II at the probed redshift ranges. These weak systems are exposed to ionizing radiation strong enough to ionize the associated carbon and silicon in them to their triply ionized state. Moreover, these high-ionization absorbers detected in the weak Mg II systems are indicative of metal-enriched material in the CGM, rather than the metal-poor infalling gas from the IGM. Whether the high-z weak (strong) Mg II systems follow the same origin pattern of corotating/infalling (outflowing) gas in the CGM as their low-z counterparts will need to wait for detailed absorber-galaxy pair kinematic analysis. We also looked at the redshift dependence of the ratios of column densities and equivalent widths between weak Mg II and highly ionized absorbers and no clear trend is observed in these systems with respect to redshift.

Studying iron abundance ratios in weak Mg II absorbers can provide further clues to their origin. 21 weak Mg II absorbers at $2.5 < z < 6.3$ are associated with Fe II whose log $(N_{\rm Fe\,II}/N_{\rm Mg\,II})$ values range between –0.75 to 0.1. Among these Fe II–Mg II associations, three are found to be iron-rich (log $(N_{\rm Fe\,II}/N_{\rm Mg\,II}) \geq 0$) as shown in Fig. 9. There appears to be an anticorrelation between the column density ratios of the absorbers and the redshift. The iron-rich systems above the dashed horizontal line seem to disappear at $z > 4.5$, but this might be due to the relatively small number of absorbers detected at higher redshifts. A K-S test of the systems at $z < 4.5$ and $z > 4.5$ yielded a p-value of 0.15 showing that $z > 4.5$ and $z < 4.5$ Mg II absorbers most probably arise from the same parent population. A similar anticorrelation has been reported by Narayanan et al. (2008) in a study of weak Mg II absorbers at $0.4 < z < 2.4$. A detailed study on the association of Mg II and Fe II might give us some hints about their absence. However, according to previous low-redshift studies on the association of weak Mg II absorbers and Fe II (Rigby et al. 2002; Narayanan et al. 2008), these iron-rich weak Mg II absorbers require enrichment from Type Ia supernovae (SNe) while the iron-poor systems require alpha enhancement from external enrichment such as bubbles and superwinds of massive galaxies or trapping of ejecta from local SNe (Rigby et al. 2002). The observed increase in alpha enhancement of weak Mg II systems with redshift shows that the most of the early galaxies traced by these systems are producing

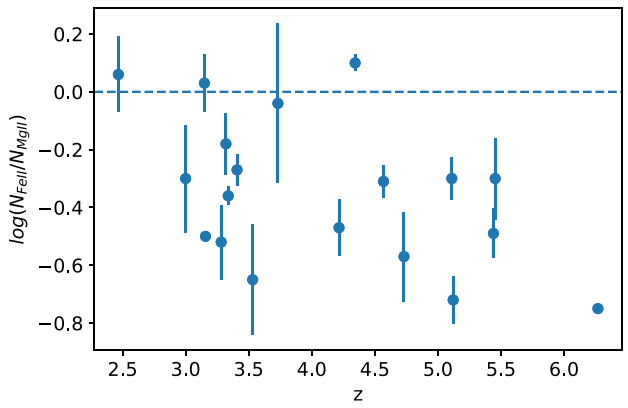

Figure 9. The ratio of column densities of Mg II and Fe II across redshift. The errors are the 1σ statistical errors in the column densities of both the ions. Out of the 21 weak Mg II absorbers, three are iron rich systems (above the dashed horizontal line) which disappear at $z > 4.5$.

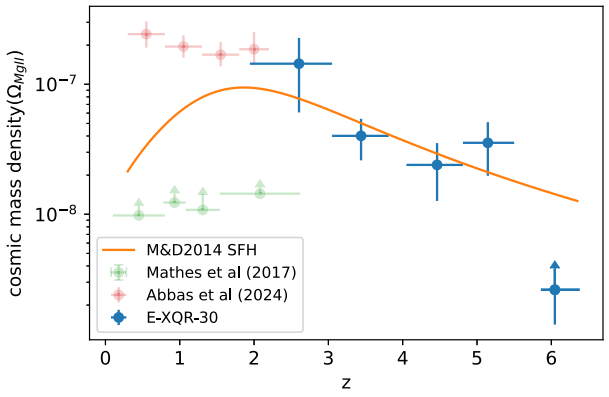

Figure 10. The figure shows the evolution of cosmic mass density of Mg II dominated by strong Mg II at $1.9 < z < 6.4$. The blue points represent the $\Omega_{\rm Mg\,II}$ and the orange line indicates the cosmic SFH from Madau & Dickinson (2014) normalized to the observations. $\Omega_{\rm Mg\,II}$ measurements at $0 < z < 2$ are also shown for comparison. It can be observed that $\Omega_{\rm Mg\,II}$ declines with redshift at $z > 3$ with little to no evolution towards $z < 3$ which is consistent with the global SFH trend. Since cosmic mass density is a mass-weighted statistic, the sharp decline in $\Omega_{\rm Mg\,II}$ at $z > 5.5$ is attributed to zero strong Mg II systems detected in the final redshift bin, as explored in Fig. 11.

more alpha elements through core-collapse SNe of massive stars in short time-scales (Thomas, Greggio & Bender 1999; Thomas et al. 2010; Johansson, Thomas & Maraston 2012; Conroy, Graves & van Dokkum 2014; Segers et al. 2016). Nevertheless, galaxies associated with the iron-rich systems in our sample likely result from stellar products over longer time-scales, possibly in the inner haloes of massive quiescent galaxies (Zahedy et al. 2017).

4.2 Strong Mg II absorbers and star formation history

There have been a handful of previous works showing the potential of strong Mg II absorbers in tracing the SFH of the Universe. Earlier works of strong Mg II have found out that there are correlations between the equivalent width of the absorber and the blue host galaxy colour (Zibetti et al. 2007; Lundgren et al. 2009; Noterdaeme et al. 2010; Bordoloi et al. 2011; Nestor et al. 2011). Strong Mg II absorbers are also observed to be associated with star-forming galaxies from their spectroscopic observations (Weiner et al. 2009; Rubin et al. 2010). Studies by Kacprzak et al. (2012) and Nielsen et al. (2015) on the azimuthal angle dependence of Mg II have shown that strong Mg II absorbers are found along the minor axis of face-on red galaxies tracing outflows from galaxies. On the contrary, there also exist studies like Bouché et al. (2016) and Zabl et al. (2019) showing that Mg II absorbers are aligned with the galactic discs but at a lower incidence rate, tracing the inflows. Ménard et al. (2011) formulated a scaling relation between the median O II luminosity surface density and the equivalent width of the Mg II absorbers at $0.4 < z < 1.3$ and showed that strong Mg II absorbers are powerful tracers of star formation independent of redshift and not remarkably affected by dust extinction. Near-IR spectroscopic surveys such as Matejek & Simcoe (2012) and C17 showed that the decline in cosmic SFR after the reaching the peak at $z \sim 2$, is reflected in the observed decline in the comoving line density of strong Mg II at $z > 2$. They used the scaling relation from Ménard et al. (2011) to estimate the SFR from Mg II equivalent widths and found them to be in agreement with the observed SFR calculation from *Hubble Space Telescope* (Bouwens et al. 2010, 2011). Moreover, many previous works on Mg II absorbers such as Prochter et al. (2006), Zibetti et al. (2007), Lundgren et al. (2009), Noterdaeme et al. (2010), Bordoloi et al. (2011), and Nestor et al. (2011) conclude that strong Mg II absorbers arise in galactic outflows.

In the E-XQR-30 sample of 280 intervening Mg II absorbers, 53 absorbers have $W > 1.0$ Å and due to the improved sensitivity of X-SHOOTER, we were able to measure the column densities of these absorbers. Consequently, the cosmic mass density ($\Omega_{\rm Mg\,II}$ – mass of the absorber per unit comoving Mpc/critical density of the Universe) of the strong absorbers can be calculated using the following equation based on the approximation of Storrie-Lombardi, McMahon & Irwin (1996)

$$\Omega_{\rm Mg\,II} \simeq \frac{H_0 m_{\rm Mg}}{c\rho_{\rm crit}\Delta X}\Sigma_i \frac{N_{{\rm total},i}}{C(z, \log N_i)}, \tag{9}$$

where H_0 is the Hubble constant, $m_{\rm Mg}$ is the atomic mass of magnesium, $\rho_{\rm crit}$ is the critical density of the Universe, $N_{{\rm total},\,i}$ is the column density of the absorbers in the ith log N bin, and $C(z, \log N_i)$ is the completeness correction. The errors associated with $\Omega_{\rm Mg\,II}$ is computed using the equation below from Storrie-Lombardi et al. (1996)

$$\left(\frac{\delta\Omega_{\rm Mg\,II}}{\Omega_{\rm Mg\,II}}\right)^2 = \frac{\Sigma(N^2)}{(\Sigma N)^2}. \tag{10}$$

In the literature, $\Omega_{\rm Mg\,II}$ has been compared with the cosmic SFH evolution, since both are functions of volume density. However, our long lever arm from $2 < z < 6$ highlights the differences between the two measures: The turnover in cosmic SFR at $z \sim 2$ is contrasted with the cosmic mass density of the Mg II ion, a fraction of total metal density, which is monotonic over time. Our results on the cosmic mass density of Mg II at $2 < z < 5.5$ agree well with the trend in the global star formation rate density from Madau & Dickinson (2014) that has been normalized to the $\Omega_{\rm Mg\,II}$ measurements, as shown in Fig. 10. The values are tabulated in Table 1. The blue points refer to the cosmic mass density measurements from this work, and the orange curve represents the best-fitting function for the global SFH from Madau & Dickinson (2014) at $0.3 < z < 6.4$. The light green points are $\Omega_{\rm Mg\,II}$ from Mathes et al. (2017) and the light red points are from Abbas et al. (2024) for $z < 2$. It can be observed that the mass density shows little to no-evolution for $z \leq 2$. As can be seen in Fig. 10, the mass densities from Mathes et al. (2017) is an order of magnitude lower than those from Abbas et al. (2024). This is

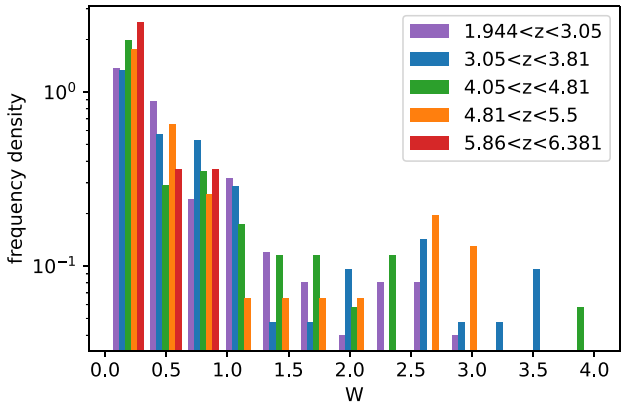

Figure 11. The rest-frame equivalent width distribution for Mg II that is colour coded based on the redshift interval to which the absorbers belong. The W bins have a binwidth of ∼0.3 Å where each bin in each redshift interval has a binsize of ∼0.05 Å. The histogram is normalized to the total absorber counts in such a way that the area under the histogram equals to 1. The absorbers at all redshifts peak at $W < 0.5$Å; showing that majority of the absorbers in the E-XQR-30 sample are weak. As we progress to larger equivalent widths of $W > 1.0$Å; absorbers at $z > 5.86$ disappear indicating an absence of high-z strong Mg II systems.

because Mathes et al. (2017) used the apparent optical depth method to measure the column densities of Mg II systems, which provides only lower limits for unresolved saturation and therefore, should be viewed as lower limits (Abbas et al. 2024). Overall, the cosmic mass density of Mg II shows little evolution from redshift 0 to 3, followed by a drop in $\Omega_{\rm Mg\,II}$ at $z > 3$ which is consistent to the expected trend in the metal content evolution of the Universe from the global SFH (see Madau & Dickinson 2014, fig. 14). As expected, there is a lag between SFR and metals appearing in the CGM (see fig. 6 in Davies et al. 2023b for examples of the predicted rate of change in metal content flowing through to the measurement of $\Omega_{\rm C\,IV}$). The peak in the metal mass density is anticipated to be at lower redshifts than the peak in the global SFH and therefore, the slight rise in $\Omega_{\rm Mg\,II}$ after the cosmic noon is consistent with the cosmic SFH trend. Nevertheless, Ménard et al. (2011) have shown that strong Mg II trace a substantial fraction of global star formation at redshifts $z < 2$ based on an SDSS survey. Though $\Omega_{\rm Mg\,II}$ from this work hints at a sudden drop in mass density at $z > 5.5$ due to the absence of strong Mg II, the small ΔX of the final redshift bin means that the null detection of strong absorbers is not statistically significant. A more detailed analysis of the relation between SFH and metal absorbers will be discussed in an upcoming work on galaxy-absorber pairs.

Although strong Mg II absorbers are subdominant at all redshifts compared to weak absorbers, their complete absence at $z > 5.86$ in the E-XQR-30 sample warrants investigation. On one hand, C17 detected 1 intervening strong Mg II absorber at $z > 5.9$ in one (J1048–0109 at $z \sim 6.64$; not included in the E-XQR-30 sample) among 28 quasar spectra at these redshift ranges. On the other hand, Keating et al. (2016) struggled to reproduce strong Mg II absorbers at $= 6$ in their simulated spectra. However, there are no strong absorbers at $z > 5.8$ in our sample as can be found in the histogram showing equivalent widths of Mg II in different redshift intervals in Fig. 11.

The same redshift intervals used in the dn/dX analysis of the Mg II absorbers are applied here in the histogram where the binsize for W is ∼0.3 Å that are sub-divided into bins of size ∼0.05 Å for each redshift interval. However, this is not sufficient evidence to conclude that strong Mg II absorbers are completely absent in the early Universe. There exist both possibilities of strong absorbers being either rare or less detected at higher redshifts. The initial step to investigate the absence of strong absorbers at high redshift is to check whether it is feasible to find strong absorbers at $z > 5.86$ assuming that the equivalent width distribution is constant at all redshifts. The analysis yielded an expectation value of detecting three strong absorbers at $z > 5.86$. Using a Poisson distribution with the mean value as the expected number of strong absorbers at $z > 5.86$, the probability of detecting no strong absorbers at $z > 5.86$ is calculated, giving a value of 7 per cent. This points out that the non-detection of strong absorbers at $z > 5.86$ is not statistically significant.

Other properties of the strong Mg II absorbers were investigated, including their association with high-ionization absorbers and Fe II. The medium and strong Mg II absorbers have fewer detections of associated C IV and Si IV in comparison with the weak absorbers because most of the strong Mg II absorbers in the E-XQR-30 sample are present at $z < 4$ (see Table 4) at which C IV and Si IV are inaccessible. However, the fractions of strong Mg II associated with C IV and Si IV are higher (76 and 40 per cent, respectively) than weak absorbers; possibly indicating that these dense systems located closer to the galaxies (see Section 4.3) are probably fragments from highly energetic galactic outflows. Among the few detections, most of them have higher column densities of Mg II relative to high-ionization absorbers. Apart from being Mg II enhanced, the strong absorbers outnumber the weak Mg II absorbers for their associations with Fe II and have more iron-rich systems than weak absorbers. The increased number of iron rich systems among strong Mg II absorbers can imply their origins in Type Ia SNe driven galactic superwinds.

On a side note, medium Mg II absorbers ($0.3 < W < 1.0$ Å) might be tracing the same objects as those of the weak Mg II absorbers at high redshifts due to the similar trend in their comoving line density as observed in Fig. 3. But, certain aspects, such as relatively larger number of medium systems with high column density ratios of Mg II over high-ionization absorbers and higher number of iron rich systems, when compared to the weak absorbers, tend to place the medium absorbers somewhere in between the weak and strong absorber properties.

4.3 Low-ionization absorbers evolution: chemical enrichment or ionizing background?

The comoving line density evolution of LIAs from E-XQR-30 metal absorber catalogue is a useful probe in understanding the chemical enrichment of the Universe and the strength of ionizing radiation after the EoR. The general trend observed in the evolution of these absorbers is that they increase towards high redshifts. The dn/dX of C II (Fig. 5) and O I (Fig. 7) shows an upturn at $z > 5.7$. The Mg II absorbers, which are observed to arise in different neutral hydrogen column densities from $15.5 < \log N({\rm H\,I})/{\rm cm}^2 < 20.5$ (Bergeron & Stasińska 1986; Steidel & Sargent 1992; Churchill et al. 2000), trace a range of ionization states whose collective number densities decline with increase in redshift (Fig. 1).

One of the most intriguing questions about the LIAs at high redshift is about the properties of these systems in the early Universe. There have been many works trying to identify what these absorbers are associated with and how different they are from the low-redshift absorber populations. Following C19, we use H I column density distribution function ($f(N_{\rm H\,I}, X) = \frac{\partial^2 n}{\partial n \partial X}$) from the literature for DLAs at $2.0 < z < 5.0$ in Noterdaeme et al. (2009) to compare with the dn/dX of LIAs. The gamma function fit from Noterdaeme et al. (2009) has been used here because this work uses a large

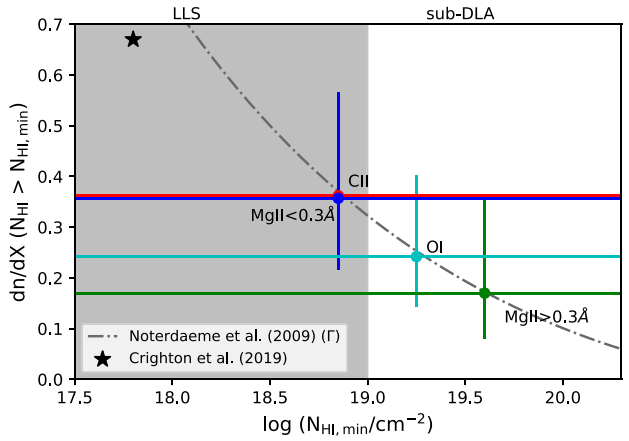

Figure 12. The DLA incidence rate as a function of the lowest H I column density using the H I column density distribution functions at $2 < z < 5$ in order to test the C19 hypothesis of LIAs as analogues of metal poor DLAs and sub-DLAs. The grey dot–dashed curve shows the DLA distribution from previous literature as indicated in the plot. But due to the flattening of $f(N_{H\,I},X)$ at the Lyman limit, the extrapolation of a single power law could be associated with large uncertainties towards $N_{H\,I} < 10^{19}\mathrm{cm}^{-2}$. The black star marks the dn/dX of LLS at $z = 5.05$ from Crighton et al. (2019). The solid horizontal lines mark the incidence rate of the LIAs at $z > 5.7$, different ion represented by a different colour. The grey-shaded region represents the LLS column densities while the unshaded region shows the sub-DLA region. It can be seen that the comoving line density of each metal ion corresponds to a different absorber class based on the minimum H I column density. The figure shows that O I and stronger Mg II absorbers have a similar comoving line density to the sub-DLAs in O'Meara et al. (2007). However, the higher incidence rates of C II and weak Mg II absorbers correspond to H I absorbers that sit between the LLS and sub-DLA systems.

sample of DLAs compared to other DLA studies in the literature and moreover, the extrapolation of the function reproduces the sub-DLA distribution. Fig. 12 depicts the incidence rate of DLAs and sub-DLAs as a function of the lowest H I column density. The dot–dashed curve represents the DLA comoving line density obtained by integrating $f(N_{H\,I}, X)$ over a range of column densities. However, an extrapolation of the DLA distribution by a single power law may not be the best to represent the frequency distribution of H I column densities at $z \sim 5$ all the way down to $N_{H\,I} < 10^{19}\mathrm{cm}^{-2}$ due to the flattening of $f(N_{H\,I},X)$ at the start of the optically thick regime at the Lyman limit (Crighton et al. 2019). The dn/dX of LLS from Crighton et al. (2019) at $z \sim 5$ is shown in Fig. 12 using a black star and it does not coincide with the extrapolated DLA distribution. Each of the horizontal lines in the figure corresponds to different LIAs comoving line density at $z > 5.7$ from this work. It is evident that the minimum hydrogen column density required to reproduce the observed comoving line density decreases from stronger Mg II ($W > 0.3$ Å) to O I and then to C II and weak Mg II ($W < 0.3$ Å). The dn/dX values of C II and Mg II are higher than the previous surveys of C19 and C17 due to increased sensitivity and completeness correction of our survey.

If the LIAs follow the $f(N_{H\,I},X)$ distribution of DLAs in Noterdaeme et al. (2009), then the minimum column density of hydrogen required to reproduce the observed number densities for O I, log $N_{H\,I,min}/\mathrm{cm}^2 \gtrsim 19.25$; for C II and weak Mg II, log $N_{H\,I,min}/\mathrm{cm}^2 \gtrsim 18.85$ and for stronger Mg II, log $N_{H\,I,min}/\mathrm{cm}^2 \gtrsim 19.60$. O I and stronger Mg II fall in the sub-DLA category (in agreement with the predictions of Becker et al. (2011) for O I and C19 for stronger Mg II where they used the dn/dX from C17). We present additional evidence for O I tracing sub-DLAs, dn/dX for O I at $z > 5.7$ is $0.24^{+0.16}_{-0.10}$ which is close to the combined number density of DLA and sub-DLA over $3 < z < 5$ (O'Meara et al. 2007; Noterdaeme et al. 2009; Prochaska & Wolfe 2009; Crighton et al. 2015). Weak Mg II and C II fall in the LLS category contrary to the prediction of C19 where they used the dn/dX value for C II from their work. C19 predicted the high-redshift C II systems existing as DLAs and sub-DLAs. Dividing the Mg II sample based on their equivalent widths, the weak absorbers with dn/d$X = 0.357$ falls within the column densities of LLS or super-LLS (sub-DLAs) systems probably tracing the infalling and co-rotating gas in the galaxy haloes as predicted by Kacprzak et al. (2011, 2012); Nielsen et al. (2015). The medium absorbers fall in the sub-DLA systems and for the strong absorbers, there are no detections at $z > 5.7$, but by using the upper limit (see Table 2), they correspond to the H I column density of sub-DLAs. Thus, it is an additional evidence apart from the histogram in Fig. 11, for the incidence rates of Mg II being largely dominated by the weak absorbers at high z. As the equivalent width of the Mg II absorbers decreases, they tend to be increasingly ionized. This is also supported by the work of Nielsen et al. (2013) where they showed an anticorrelation between the equivalent width of the Mg II systems and the impact parameter and thus, exposing the weaker absorbers more to the ionizing UV background. Moreover, Stern et al. (2016) found that the density profile of the cool gas scales inversely with distance from the galaxy centre manifesting that the strong LIAs lie close to the galaxy itself.

We also tried to obtain neutral hydrogen column densities of Mg II systems using the scaling relations in Ménard & Chelouche (2009) and Lan & Fukugita (2017) in order to compare with the log $N_{H\,I,min}/\mathrm{cm}^2$ values obtained from Fig. 12. According to Lan & Fukugita (2017), the scaling relation between Mg II equivalent width and H I column density is

$$N_{H\,I} = A\left(\frac{W_{\lambda 2796}}{1\text{Å}}\right)^{\alpha}(1+z)^{\beta}, \tag{11}$$

where $\alpha = 1.69 \pm 0.13$, $\beta = 1.88 \pm 0.29$, and $A = 10^{18.96\pm0.10}\,\mathrm{cm}^{-2}$. Applying this equation to our weak Mg II data, we obtain $\log N_{H\,I,min}/\mathrm{cm}^2 = 19.22$ and for Mg II with $W \geq 0.3$ Å; $\log N_{H\,I,min}/\mathrm{cm}^2 = 20.18$. These values are very close to the inferred neutral hydrogen column densities in Fig. 12. Previously, using low-redshift ($z < 1.65$) Mg II absorbers with $W > 0.3$ Å; Ménard & Chelouche (2009) developed a scaling relation given as

$$\langle N_{H\,I}\rangle_g(W_0) = C_g(W_0)^{\alpha_g}, \tag{12}$$

where $C_g = (3.06 \pm 0.55) \times 10^{29}\,\mathrm{cm}^{-2}$ and $\alpha_g = 1.73 \pm 0.26$. Applying this relation to weak and stronger absorbers provided us with H I column densities for weak absorbers as log $N_{H\,I,min}/\mathrm{cm}^2 = 18.12$ and for stronger absorbers, log $N_{H\,I,min}/\mathrm{cm}^2 = 19.11$. These results are almost one order of magnitude lower than the values from Fig. 12 which might be because Ménard & Chelouche (2009) based their analysis only on low-redshift stronger absorbers.

Having seen that the weak Mg II and C II have similar H I column densities, it is important to understand more about their ionization conditions by looking at their association with high-ionization absorbers such as C IV and Si IV (In this analysis, we have considered only those C II and O I absorbers that can be detected across the redshift range where the associated ions are detected). We found that 50 per cent (11/22) of C II systems have both C IV and Si IV across $4.317 \leq z \leq 6.339$ and $4.907 \leq z \leq 6.339$, respectively. The C II–C IV association is closer to weak Mg II-C IV (43 per cent) while the fraction of C II with Si IV is almost double the fraction of weak Mg II–Si IV (25 per cent) association. Similarly, we analysed the association

of O I with high ionization species to compare with the ionization conditions of stronger Mg II with $W > 0.3$ Å; 38 per cent (3/8) of O I absorbers is associated with C IV while 25 per cent (2/8) of O I absorbers have Si IV association. Therefore, fraction of O I with C IV is more than half of stronger Mg II–C IV (59 per cent) systems while the fraction of O I absorbers associated with Si IV is almost similar to stronger Mg II (29 per cent). Overall, weak Mg II & C II and stronger Mg II & O I have similar ionization conditions although both ions in each pair appearing in the same systems is very rare. Only 5 out of 22 C II has weak Mg II associated with them while 3 out of 10 O I systems are detected with stronger Mg II at a redshift range of $5.169 < z < 6.381$.

As one would expect, the Universe was largely neutral right after the formation of the first stars and galaxies during the EoR. The LIAs, especially C II and O I trace neutral regions of the CGM that are slightly ionized. Nevertheless, C II is also found in somewhat ionized gas, more so than O I. The ionization potential of these absorbers is less than 13.6 eV and therefore, they are not self-shielded by hydrogen and appear as singly ionized species in an otherwise neutral medium (Becker et al. 2015a). An increasing trend in the comoving line density of the LIAs towards high redshift indicates that some changes are happening to the ionizing radiation at $z \gtrsim 5.7$. In the early Universe, the ionizing radiation is not strong enough to produce highly ionized absorbers in the metal-poor CGM and as a result, there existed a combined effect of low-metallicity and weak-ionizing photons towards the tail end of EoR responsible for the observed trends in C II and O I.

The rising trend in the comoving line density of C II in this work provides further evidence to the findings of C19 in which the high-redshift absorbers are found to be dominated by the low-ionization species. Furthermore, Davies et al. (2023b) also found that the comoving line density of C IV declines with increasing redshift using E-XQR-30 sample concurring with the work of C19. The presence of a weaker or softer ionizing background can produce an increase in C II and a decrease in C IV content at high z. Furthermore, an upturn is observed for O I absorbers at $z > 5.7$ from the E-XQR-30 sample when combined with the results of B19 at $z < 5.7$. Due to the similar ionization potential of O I as of neutral hydrogen, it traces gas that is largely neutral. Therefore, its decline at $z < 5.7$, points to the decline of the neutral regions and the transition of metals in the galaxy haloes to higher ionization states due to the ongoing reionization process at $z \sim 6$.

The upturn in the O I comoving line density suggests a rapid change in the ionization state of the CGM which can be produced by an external ionizing source rather than the host galaxy. According to Harikane et al. (2018, 2022), no significant changes are reported in the galaxy properties at $2 < z < 7$ that would otherwise potentially create a rapid inside-out ionization of the CGM gas. Moreover, B19 discusses the possibility of simultaneous reionization of the CGM and IGM and also an alternative scenario where the CGM remains self-shielded for a while when the local IGM undergoes reionization. In the second scenario, the ionization of the CGM occurs towards the tail end of EoR when the mean free path of photons increases (Fan et al. 2006; Becker et al. 2021; Gnedin & Madau 2022; Gaikwad et al. 2023; Zhu et al. 2023), exposing the region to photons from distant sources. The rapid change in the ionization state of the galaxy haloes is further supported by the abrupt increase in the volume-averaged neutral hydrogen fraction across $5.7 < z < 6.4$ (similar to the redshift range of O I where an upturn is found) shown with a fully coupled radiative hydrodynamic simulation known as Cosmic Dawn III by Lewis et al. (2022). Additional evidence for this rapid increase can be found in Gaikwad et al. (2023), where they used quasar absorption spectra from XSHOOTER and ESI and modelled the fluctuations in ionizing radiation field using the post-processing simulation code 'EXtended reionization based on the Code for Ionization and Temperature Evolution'. All these simulations and observations including this work, collectively point out that the ionizing radiation underwent a significant strengthening at $z < 5.7$ and predicts a late end of EoR towards $z \sim 5.3$. The rapid increase observed in the comoving line density of O I across both $z > 5.3$ and 5.7 (see Fig. 7 and Table 4) from this work points to persisting fluctuations in neutral hydrogen fraction until $z \sim 5.3$. A late end to the EoR has also been observed by the recent works of Zhu et al. (2021) and Bosman et al. (2022) using the quasar spectra from E-XQR-30.

Oppenheimer et al. (2009) employed the column density ratios of aligned absorber as a statistical tool to compare the different ionization models. Applying similar technique to our observations, we plot the column density ratios of C II and O I that fall in the same system as defined by our survey in Fig. 13(a) to compare it with the three models from Oppenheimer et al. (2009). 8/22 C II absorbers are aligned with O I while 8/10 O I absorbers are associated with C II. The remaining two O I absorbers are also aligned with C II, however, those two C II absorbers are coincident with BAL regions of the quasar and therefore, are not included in the primary sample of the E-XQR-30 catalogue. Thus, the alignment fraction of C II with O I is 36 per cent and O I with C II ranges from 80 to 100 per cent.

If the Universe was fully neutral at $z \sim 6$ with no ionizing background existing below the Lyman limit, we would expect a large fraction of C II absorbers to show associated O I absorption but this is not the case in our work. We have only detected 22 C II and 10 O I intervening absorbers in the primary sample at $5.2 < z < 6.4$. In the second scenario, the Universe is assumed to have been fully ionized with a spatially uniform background everywhere and the third case is a patchy reionization model. Fig. 13(b) clearly demonstrates that the fraction of C II aligned with O I and vice versa from the simulation for the patchy reionization model is in agreement with the observed alignment fractions. The hatched bins represent the alignment fractions of different reionization models from Oppenheimer et al. (2009) and the colour filled bins represent the observed ratios from this work. Therefore, our results favour a patchy reionization rather than a spatially homogeneous ionizing background. Moreover, the non-detection of O I in many sightlines where C II and other high ionization species are detected, indicate that those sightlines probe ionized regions while others pass through metal-enriched neutral gas close to the galaxies. A caveat to the reionization models in Oppenheimer et al. (2009) is that those models are not based on a radiative transfer simulation, so self-consistently accounting for self-shielding could change the alignment results.

Using the Technicolor Dawn simulations, Finlator et al. (2018), produced a spatially inhomogeneous reionization model for the galaxy-driven reionization scenario where they compare their simulated equivalent width distribution with the then existing observations for C II and O I such as Becker et al. (2011) and Bosman et al. (2017). They found that the simulations overproduced weaker systems and underproduced strong systems. However, using data from E-XQR-30, we computed the W distribution by calculating the comoving line densities for absorbers with different minimum equivalent widths as shown in Fig. 14. The top panels show the distribution for C II equivalent widths and the bottom panel demonstrates the equivalent width distribution for O I. The blue histograms indicate the observed distribution from this work while the orange histograms

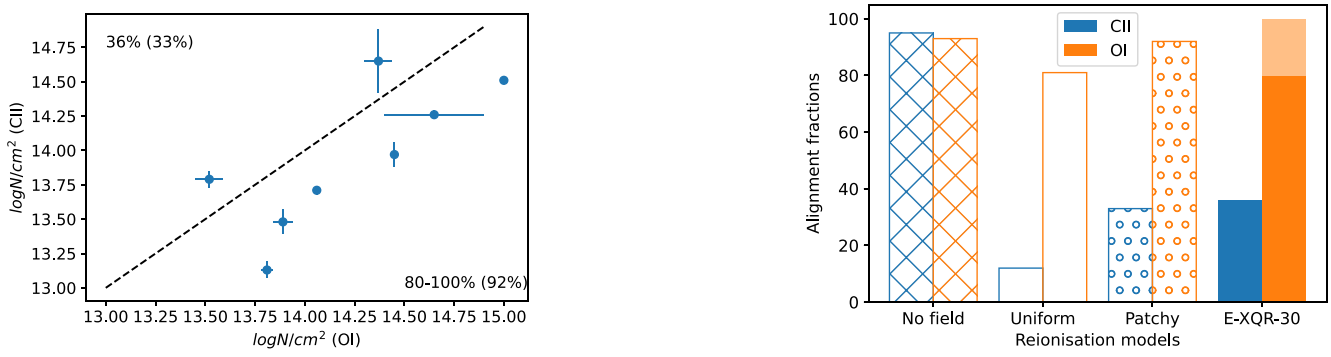

(a) (b)

Figure 13. The left panel represents the column density ratios of C II and O I that are aligned to each other within a single system. The upper right corner in the figure shows the alignment fraction of C II with O I (8/22) and the lower right shows the alignment fraction of O I with C II (8-10/10). The values in brackets refer to the fractions from the simulations for a patchy reionization model in Oppenheimer et al. (2009). The right panel shows the comparison of alignment fractions from different reionization models in Oppenheimer et al. (2009) with the observed absorber ratios from E-XQR-30 and our results favour a patchy reionization model.

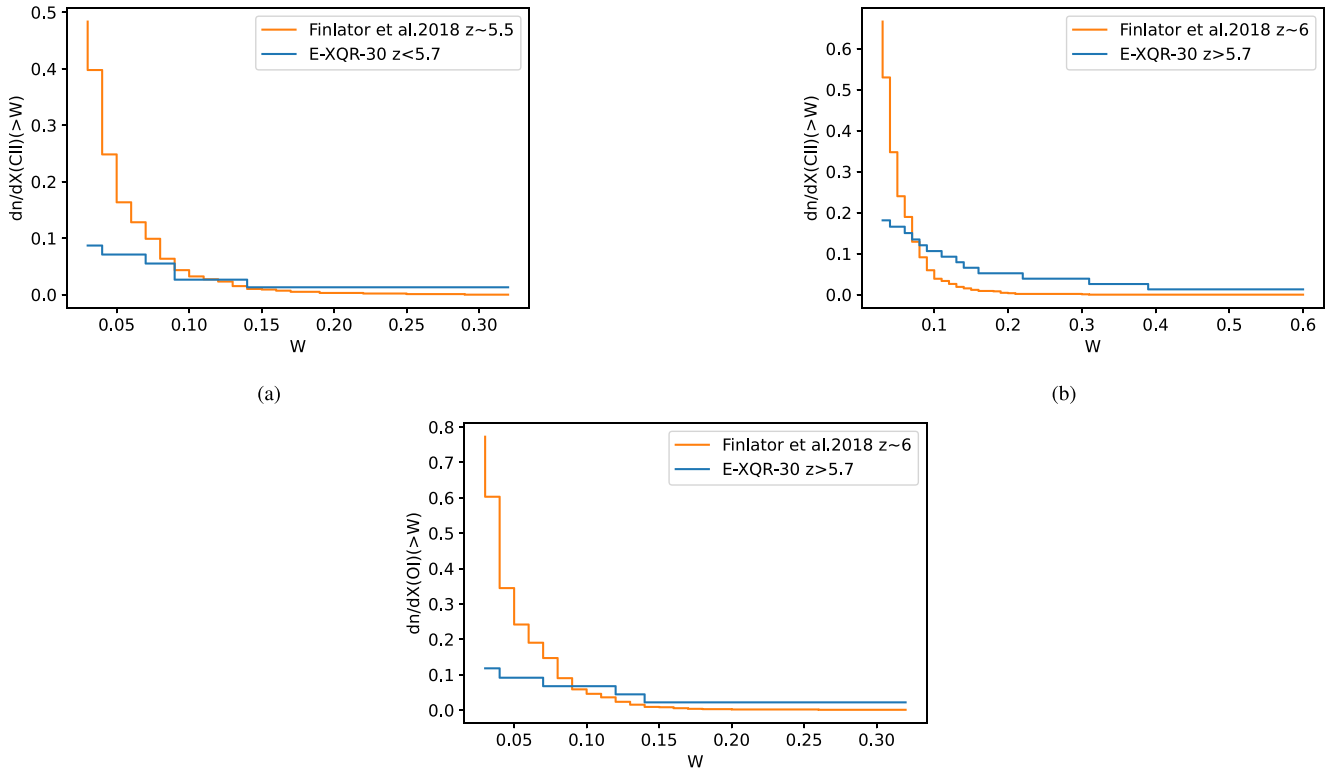

(a) (b)

(c)

Figure 14. The equivalent width distribution for low-ionization species for comparison with simulations from Finlator et al. (2018). The top panels show the distribution for C II and the bottom panel illustrates the distribution for O I. The orange-coloured histogram represents the model from Finlator et al. (2018) while the blue histogram stands for the results from this work. It can be seen that both C II and O I data have been divided into redshift intervals for appropriate comparison with the simulations at those redshifts. The simulations overpredict the weak absorbers while they agree with the observed distribution towards higher equivalent widths at $W > 0.1$ Å. For O I, comparison of the simulations with the lower redshift sample is not shown here due to very small number of absorbers at $z < 5.7$.

show the simulated distribution from Finlator et al. (2018). The observed equivalent widths for C II and O I have been divided at $z \sim 5.7$ for comparison with the corresponding simulations. However, histograms comparing O I distribution at $z < 5.7$ is not included in the figure because there are not enough absorbers at this redshift range. Comparing with simulations from Finlator et al. (2018), the model

overpredicts the weak absorbers but is in agreement towards higher equivalent widths at $W > 0.1$ Å; for both C II and O I. Therefore, the distribution from our work agrees better with the simulations when compared to the earlier works. The over prediction of weak absorbers in the simulation could be due to issues related to CGM metallicity, wind speed and UV background (Finlator et al. 2018).

5 CONCLUSIONS

The evolution of LIAs, namely Mg II, C II, and O I, across redshift is studied using the E-XQR-30 metal absorber catalogue prepared by Davies et al. (2023a) from 42 high S/N and intermediate resolution XSHOOTER quasar spectra at $z \sim 6$. The catalogue consists of a total of 778 systems including 260 Mg II, 22 C II and 10 O I intervening absorbers separated from the background quasar by $>10\,000$ km s^{-1}. The E-XQR-30 has significantly increased the path-length of $z \sim 6$ C II and O I by 50 per cent as well as the sample size of high-redshift metal absorbers compared with previous large surveys of high-redshift metal absorbers. For example, 131 weak Mg II ($W < 0.3$ Å) absorbers at $z > 2$ are detected for the first time indicating the improved sensitivity of E-XQR-30 over other high-redshift metal absorber surveys. The sample completeness is generally high, reaching 50 per cent completeness at $W > 0.03$ Å.

Mg II absorbers, altogether, decline in comoving line density (dn/dX) towards high redshift with the dn/dX of weak and medium absorbers remaining constant across redshift while the dn/dX of strong absorbers decline with redshift. The cosmic mass density of Mg II ($\Omega_{\rm Mg\,II}$) dominated by the strong Mg II absorbers follows the declining trend in the global SFH across $2 < z < 5.5$. This is evidence that strong absorbers mimics the SFR evolution suggesting a connection between star formation and CGM enrichment rates. The weak Mg II sample in E-XQR-30 is of great significance as this is the first ever detection of a substantial size of population of these absorbers at $2 < z < 6$. For weak Mg II systems to continue to trace sub-LLS environments to high redshift, their covering fraction must decline by factor of 3 as redshift 6 is approached. Their associations with Fe II and high-ionization absorbers such as C IV and Si IV have also been studied, respectively, in this work, providing insights into possible scenarios for the enrichment of these weak absorbers. The column density ratios of Fe II over weak Mg II indicates that they retained their enrichment mostly from core-collapse SNe of early stars particularly at $z > 4.5$. C IV and Si IV associations indicate that these systems have high-column densities of highly ionized absorbers and therefore, are exposed to ionizing radiation more than strong absorbers. The C II absorbers tend to increase with increasing redshift and the O I absorbers show an upturn at $z > 5.7$. The results obtained in this work is consistent with what has been observed in the previous high-redshift surveys, in particular, C17 for Mg II, C19 for C II, B19 for O I and *JWST* results from Christensen et al. (2023) and emphasize the need for higher resolution spectroscopy to detect metal absorbers.

The redshift evolution of metal absorbers provides information about the chemical enrichment of the Universe towards the tail end of EoR and the nature of ionizing radiation that ionized the neutral hydrogen in the CGM and IGM. The overall trend in the LIAs suggests a weaker UV ionizing radiation at $z > 5$. As more galaxies formed, the metal content of the Universe increased through stellar nucleosynthetic processes and was ejected into the surrounding media. The results also favour the assumption of reionization of galaxy haloes from external sources rather than *in situ* sources. If the CGM is reionized by the host galaxies, then the ionization in CGM would tend to respond to the host galaxy properties in place of global evolution in the UV background. The decline in O I at $z < 5.3$ can also be related to the intensifying of the ionizing UV background towards $z < 5.3$ and such a strengthening is expected only towards the end of reionization. Therefore, the rapid rise in the comoving line density in the LIA evolution also supports the recent studies proposing a late end of reionization, probably at $z \sim 5.3$. Furthermore, our results provide evidence for this late reionization continuing to occur in metal-enriched and therefore biased regions of the Universe.

The reionization of the Universe is still continuing to be an intriguing question for astronomers which created a major landmark in the transformation of the Universe from a homogeneous environment to a largely structured cosmos. The results from this work motivate future research on the relative role of chemical enrichment and nature of the UV background, both strength and hardness of the photons, during the early epochs which shaped the Universe as we see it today. This can be analysed by extending the sample size of C II absorbers that has a shorter path-length with the help of a proxy and looking at the ratios of the low and high ionization states of carbon. The addition of more sightlines to deeper redshifts will also provide additional evidences to validate the current assumptions on the nature of reionization. Also, with the help of Multi Unit Spectroscopic Explorer (MUSE; for e.g. Díaz et al. 2021), Atacama Large Millimetre/submillimetre Array (*ALMA*; for e.g. Kashino et al. 2023) and *JWST* (for e.g. Bordoloi et al. 2023), images and spectra of galaxies associated with the high-redshift absorbers can be obtained using which the nature of the galaxies producing these absorbers in the early Universe can be identified.

ACKNOWLEDGEMENTS

The authors thank the referee for providing valuable feedback. This research was supported by the Australian Research Council Centre of Excellence for All Sky Astrophysics in 3 Dimensions (ASTRO 3D), through project number CE170100013. Based on observations collected at the European Organisation for Astronomical Research in the Southern Hemisphere under ESO Programme IDs: 0100.A- 0625, 0101.B-0272, 0102.A-0154, 0102.A-0478, 084.A-0360(A), 084.A-0390(A), 084.A-0550(A), 085.A-0299(A), 086.A-0162(A), 086.A-0574(A), 087.A-0607(A), 088.A-0897(A), 091.C-0934(B), 096.A-0095(A), 096.A-0418(A), 097.B-1070(A), 098.B-0537, 098.B-0537(A), 1103.A-0817, 294.A-5031(B), 60.A-9024(A) and AMS acknowledges the XQR-30 collaboration involved in taking the observations and reducing the data. This work used NASA's Astrophysics Data System as well as MATPLOTLIB (Hunter 2007), NUMPY (Harris, Millman & van der Walt 2020) and SCIPY (Jones et al. 2001).

AMS acknowledges Asif Abbas for providing the results on cosmic mass density of Mg II at low redshift before publishing and the literature values for dn/dX of Mg II. AMS also acknowledges Kristian Finlator for providing comparison data from the simulations for the equivalent width distributions of O I and C II.

For the purpose of open access, LCK has applied a Creative Commons Attribution (CC BY) licence to any Author Accepted Manuscript version arising from this submission.

GK is partly supported by the Department of Atomic Energy (Government of India) research project with Project Identification Number RTI 4002, and by the Max Planck Society through a Max Planck Partner Group.

RAM acknowledges support from the Swiss National Science Foundation (SNSF) through project grant 200020_207349.

SEIB is supported by the Deutsche Forschungsgemeinschaft (DFG) under Emmy Noether grant number BO 5771/1-1.

We also thank Nikole Nielsen, Glenn Kacprzak, Chris Churchill, and Chris Blake for valuable discussions.

DATA AVAILABILITY

The metal absorber catalogue used in this project and the PYTHON script used to calculate the absorption path and redshift intervals are publicly available and can be downloaded at: https://github.com/XQR-30/Metal-catalogue/tree/main/AbsorptionPathTool.

REFERENCES

Abbas A., Churchill C. W., Kacprzak G. G., Lidman C., Guatelli S., Bellstedt S., 2024, preprint (arXiv:2403.13184)
Bañados E. et al., 2018, Nature, 553, 473
Bahcall J. N., Peebles P. J. E., 1969, ApJ, 156, L7
Becker G. D., Bolton J. S., 2013, MNRAS, 436, 1023
Becker G. D., Sargent W. L. W., Rauch M., Simcoe R. A., 2006, ApJ, 640, 69
Becker G. D., Sargent W. L. W., Rauch M., Calverley A. P., 2011, ApJ, 735, 93
Becker G. D., Bolton J. S., Lidz A., 2015a, Publ. Astron. Soc. Aust., 32, e045
Becker G. D., Bolton J. S., Madau P., Pettini M., Ryan-Weber E. V., Venemans B. P., 2015b, MNRAS, 447, 3402
Becker G. D. et al., 2019, ApJ, 883, 163 (B19)
Becker G. D., D'Aloisio A., Christenson H. M., Zhu Y., Worseck G., Bolton J. S., 2021, MNRAS, 508, 1853
Bergeron J., Stasińska G., 1986, A&A, 169, 1
Bischetti M. et al., 2022, Nature, 605, 244
Bischetti M. et al., 2023, ApJ, 952, 44
Bordoloi R. et al., 2011, ApJ, 743, 10
Bordoloi R. et al., 2023, preprint (arXiv:2307.01273)
Bosman S. E. I., Becker G. D., Haehnelt M. G., Hewett P. C., McMahon R. G., Mortlock D. J., Simpson C., Venemans B. P., 2017, MNRAS, 470, 1919
Bosman S. E. I. et al., 2022, MNRAS, 514, 55
Bouché N. et al., 2016, ApJ, 820, 121
Bouwens R. J. et al., 2010, ApJ, 725, 1587
Bouwens R. J. et al., 2011, ApJ, 737, 90
Chambaud G., Levy B., Millie P., Tran Minh F., Launay J. M., Roueff E., 1980, J. Phys. B At. Mol. Phys., 13, 4205
Chen H.-W., Helsby J. E., Gauthier J.-R., Shectman S. A., Thompson I. B., Tinker J. L., 2010, ApJ, 714, 1521
Chen S.-F. S. et al., 2017, ApJ, 850, 188 (C17)
Choudhury T. R., Paranjape A., Bosman S. E. I., 2021, MNRAS, 501, 5782
Christensen L. et al., 2017, A&A, 608, A84
Christensen L. et al., 2023, A&A, 680, 44
Churchill C. W., Rigby J. R., Charlton J. C., Vogt S. S., 1999, ApJS, 120, 51
Churchill C. W., Mellon R. R., Charlton J. C., Jannuzi B. T., Kirhakos S., Steidel C. C., Schneider D. P., 2000, ApJS, 130, 91
Churchill C. W., Kacprzak G. G., Steidel C. C., 2005, in Williams P., Shu C.-G., Menard B.eds, IAU Colloq. 199: Probing Galaxies through Quasar Absorption Lines. Kluwer, Dordrecht. p. 24
Churchill C. W., Trujillo-Gomez S., Nielsen N. M., Kacprzak G. G., 2013, ApJ, 779, 87
Codoreanu A., Ryan-Weber E. V., Crighton N. H. M., Becker G., Pettini M., Madau P., Venemans B., 2017, MNRAS, 472, 1023
Conroy C., Graves G. J., van Dokkum P. G., 2014, ApJ, 780, 33
Cooper T. J., Simcoe R. A., Cooksey K. L., Bordoloi R., Miller D. R., Furesz G., Turner M. L., Bañados E., 2019, ApJ, 882, 77 (C19)
Crighton N. H. M. et al., 2015, MNRAS, 452, 217
Crighton N. H. M., Prochaska J. X., Murphy M. T., O'Meara J. M., Worseck G., Smith B. D., 2019, MNRAS, 482, 1456
Cupani G., D'Odorico V., Cristiani S., Russo S. A., Calderone G., Taffoni G., 2020, in Guzman J. C., J. Ibsen, eds, Proc. SPIE Conf. Ser. Vol. 11452, Software and Cyberinfrastructure for Astronomy VI. SPIE, Bellingham. p. 114521U
D'Aloisio A., Upton Sanderbeck P. R., McQuinn M., Trac H., Shapiro P. R., 2017, MNRAS, 468, 4691
D'Aloisio A., McQuinn M., Davies F. B., Furlanetto S. R., 2018, MNRAS, 473, 560
D'Odorico V., Calura F., Cristiani S., Viel M., 2010, MNRAS, 401, 2715
D'Odorico V. et al., 2013, MNRAS, 435, 1198
D'Odorico V. et al., 2022, MNRAS, 512, 2389
D'Odorico V. et al., 2023, MNRAS, 523, 1399
Davies F. B. et al., 2018, ApJ, 864, 142
Davies R. L. et al., 2023a, MNRAS, 521, 289
Davies R. L. et al., 2023b, MNRAS, 521, 314
Díaz C. G., Ryan-Weber E. V., Karman W., Caputi K. I., Salvadori S., Crighton N. H., Ouchi M., Vanzella E., 2021, MNRAS, 502, 2645
Doughty C., Finlator K., 2019, MNRAS, 489, 2755
Duffy A. R., Wyithe J. S. B., Mutch S. J., Poole G. B., 2014, MNRAS, 443, 3435
Dutta R. et al., 2020, MNRAS, 499, 5022
Eilers A.-C., Davies F. B., Hennawi J. F., 2018, ApJ, 864, 53
Fan X. et al., 2006, AJ, 132, 117
Faucher-Giguère C.-A., 2020, MNRAS, 493, 1614
Finkelstein S. L. et al., 2019, ApJ, 879, 36
Finlator K., Thompson R., Huang S., Davé R., Zackrisson E., Oppenheimer B. D., 2015, MNRAS, 447, 2526
Finlator K., Oppenheimer B. D., Davé R., Zackrisson E., Thompson R., Huang S., 2016, MNRAS, 459, 2299
Finlator K., Keating L., Oppenheimer B. D., Davé R., Zackrisson E., 2018, MNRAS, 480, 2628
Furlanetto S. R., Loeb A., 2003, ApJ, 588, 18
Furlanetto S. R., Oh S. P., 2005, MNRAS, 363, 1031
Furlanetto S. R., Hernquist L., Zaldarriaga M., 2004, MNRAS, 354, 695
Gaikwad P. et al., 2023, MNRAS, 525, 4093
Gallerani S., Ferrara A., Fan X., Choudhury T. R., 2008, MNRAS, 386, 359
Gehrels N., 1986, ApJ, 303, 336
Gnedin N. Y., Madau P., 2022, Liv. Rev. Comput. Astrophys., 8, 3
Gnedin N. Y., Becker G. D., Fan X., 2017, ApJ, 841, 26
Grazian A. et al., 2023, ApJ, 955, 17
Greig B., Mesinger A., Davies F. B., Wang F., Yang J., Hennawi J. F., 2022, MNRAS, 512, 5390
Harikane Y. et al., 2018, Publ. Astron. Soc. Japan, 70, S11
Harikane Y. et al., 2022, ApJS, 259, 20
Harikane Y. et al., 2023, ApJ, 959, 18
Harris C., Millman K., van der Walt S. e. a., 2020, Nature, 585, 357
Hennawi J. F., Davies F. B., Wang F., Oñorbe J., 2021, MNRAS, 506, 2963
Hunter J. D., 2007, Comput. Sci. Eng., 9, 90
Johansson J., Thomas D., Maraston C., 2012, MNRAS, 421, 1908
Jones E., Oliphant T., Peterson P. et al., 2001, SciPy: Open source scientific tools for Python, http://www.scipy.org/
Kacprzak G. G., Churchill C. W., 2011, ApJ, 743, L34
Kacprzak G. G., Churchill C. W., Evans J. L., Murphy M. T., Steidel C. C., 2011, MNRAS, 416, 3118
Kacprzak G. G., Churchill C. W., Nielsen N. M., 2012, ApJ, 760, L7
Kashino D., Lilly S. J., Simcoe R. A., Bordoloi R., Mackenzie R., Matthee J., Eilers A.-C., 2023, Nature, 617, 261
Keating L. C., Haehnelt M. G., Becker G. D., Bolton J. S., 2014, MNRAS, 438, 1820
Keating L. C., Puchwein E., Haehnelt M. G., Bird S., Bolton J. S., 2016, MNRAS, 461, 606
Kulkarni G., Worseck G., Hennawi J. F., 2019, MNRAS, 488, 1035
Lan T.-W., Fukugita M., 2017, ApJ, 850, 156
Lewis J. S. W. et al., 2022, MNRAS, 516, 3389
Loeb A., Barkana R., 2001, ARA&A, 39, 19
Lundgren B. F. et al., 2009, ApJ, 698, 819
Lynch R. S., Charlton J. C., 2007, ApJ, 666, 64
Lynch R. S., Charlton J. C., Kim T.-S., 2006, ApJ, 640, 81

Madau P., Dickinson M., 2014, ARA&A, 52, 415
Maiolino R. et al., 2023, preprint (arXiv:2308.01230)
Matejek M. S., Simcoe R. A., 2012, ApJ, 761, 112
Mathes N. L., Churchill C. W., Murphy M. T., 2017, preprint (arXiv:1701.05624)
Matthee J. et al., 2022, MNRAS, 512, 5960
Ménard B., Chelouche D., 2009, MNRAS, 393, 808
Ménard B., Wild V., Nestor D., Quider A., Zibetti S., Rao S., Turnshek D., 2011, MNRAS, 417, 801
Muzahid S., Fonseca G., Roberts A., Rosenwasser B., Richter P., Narayanan A., Churchill C., Charlton J., 2018, MNRAS, 476, 4965
Narayanan A., Misawa T., Charlton J. C., Kim T.-S., 2007, ApJ, 660, 1093
Narayanan A., Charlton J. C., Misawa T., Green R. E., Kim T.-S., 2008, ApJ, 689, 782
Nasir F., D'Aloisio A., 2020, MNRAS, 494, 3080
Nestor D. B., Turnshek D. A., Rao S. M., 2005, ApJ, 628, 637
Nestor D. B., Johnson B. D., Wild V., Ménard B., Turnshek D. A., Rao S., Pettini M., 2011, MNRAS, 412, 1559
Nielsen N. M., Churchill C. W., Kacprzak G. G., 2013, ApJ, 776, 115
Nielsen N. M., Churchill C. W., Kacprzak G. G., Murphy M. T., Evans J. L., 2015, ApJ, 812, 83
Noterdaeme P., Petitjean P., Ledoux C., Srianand R., 2009, A&A, 505, 1087
Noterdaeme P., Srianand R., Mohan V., 2010, MNRAS, 403, 906
O'Meara J. M., Prochaska J. X., Burles S., Prochter G., Bernstein R. A., Burgess K. M., 2007, ApJ, 656, 666
Oh S. P., 2002, MNRAS, 336, 1021
Oppenheimer B. D., Davé R., Finlator K., 2009, MNRAS, 396, 729
Osterbrock D. E., Ferland G. J., 2006, Astrophysics of Gaseous Nebulae and Active Galactic Nuclei, University Science Books
Péroux C., Howk J. C., 2020, ARA&A, 58, 363
Perrotta S. et al., 2016, MNRAS, 462, 3285
Planck Collaboration VI, 2020, A&A, 641, A6
Prochaska J. X., Wolfe A. M., 2009, ApJ, 696, 1543
Prochter G. E., Prochaska J. X., Burles S. M., 2006, ApJ, 639, 766
Rigby J. R., Charlton J. C., Churchill C. W., 2002, ApJ, 565, 743
Robertson B. E. et al., 2013, ApJ, 768, 71
Rubin K. H. R., Weiner B. J., Koo D. C., Martin C. L., Prochaska J. X., Coil A. L., Newman J. A., 2010, ApJ, 719, 1503
Segers M. C., Schaye J., Bower R. G., Crain R. A., Schaller M., Theuns T., 2016, MNRAS, 461, L102
Seyffert E. N., Cooksey K. L., Simcoe R. A., O'Meara J. M., Kao M. M., Prochaska J. X., 2013, ApJ, 779, 161
Songaila A., Cowie L. L., 2002, AJ, 123, 2183
Steidel C. C., Sargent W. L. W., 1992, ApJS, 80, 1
Stern J., Hennawi J. F., Prochaska J. X., Werk J. K., 2016, ApJ, 830, 87
Storrie-Lombardi L. J., McMahon R. G., Irwin M. J., 1996, MNRAS, 283, L79
Thomas D., Greggio L., Bender R., 1999, MNRAS, 302, 537
Thomas D., Maraston C., Schawinski K., Sarzi M., Silk J., 2010, MNRAS, 404, 1775
Tripp T. M., Lu L., Savage B. D., 1997, ApJS, 112, 1
Tumlinson J., Peeples M. S., Werk J. K., 2017, ARA&A, 55, 389
Vernet J. et al., 2011, A&A, 536, A105
Wang F. et al., 2020, ApJ, 896, 23
Weiner B. J. et al., 2009, ApJ, 692, 187
Wise J. H., Demchenko V. G., Halicek M. T., Norman M. L., Turk M. J., Abel T., Smith B. D., 2014, MNRAS, 442, 2560
Yang J. et al., 2020, ApJ, 904, 26
Yeh J. Y. C. et al., 2022, MNRAS, 520, 2757
Zabl J. et al., 2019, MNRAS, 485, 1961
Zahedy F. S., Chen H.-W., Gauthier J.-R., Rauch M., 2017, MNRAS, 466, 1071
Zhu Y. et al., 2021, ApJ, 923, 223
Zhu Y. et al., 2022, ApJ, 932, 76
Zhu Y. et al., 2023, ApJ, 955, 13
Zibetti S., Ménard B., Nestor D. B., Quider A. M., Rao S. M., Turnshek D. A., 2007, ApJ, 658, 161
Zou S. et al., 2021, ApJ, 906, 32

Table A1. The best-fitting parameters for the W distribution at different redshift ranges.

z range	Parameters	Best-fitting value	1σ errors (+,–)
1.9–4.1	Φ^*	1.39	0.06, 0.18
1.9–4.1	α	−0.57	0.05, 0.07
4.1–6.4	Φ^*	0.74	0.14, 0.094
4.1–6.4	α	−0.79	0.10, 0.07

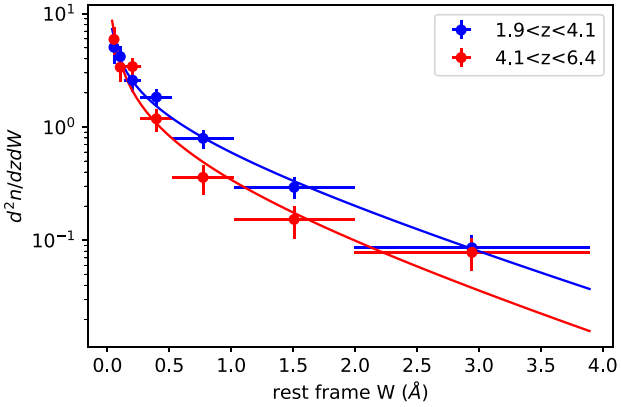

Figure A1. The equivalent width distribution fit at different redshift ranges using a Schechter function. The low-redshift values and fit are shown in blue and the high-redshift values and the fit are shown in red. The distribution is measured to steep in slope with increasing redshift.

APPENDIX A: THE REDSHIFT DEPENDENCE OF MG II EQUIVALENT WIDTH DISTRIBUTION

The exponential distribution for Mg II equivalent widths $W > 0.3$ Å has been found to steepen with redshift from the works of C17. It is important to see whether this increase in slope with redshift will be observed when weak absorbers ($W < 0.3$ Å) are also included in the sample. We attempt to fit for the equivalent widths of Mg II from E-XQR-30 with $W > 0.03$ Å across two redshift ranges; $1.94 < z < 4.05$ and $4.05 < z < 6.38$ (the absorbers in the masked redshift intervals are not included) using the Schechter function given in equation (8). Here, W^* is kept constant at 1.44 (the best-fitting W^* for the total Mg II sample) to see whether the distributions steepen with redshift.

The best-fitting parameters are given in Table A1.

The difference in parameters at different redshift intervals suggests that the equivalent distribution might not be the same at all redshifts. The fits obtained are shown in Fig. A1.

The low-redshift bin values and the corresponding fit are shown in blue while the high-redshift bin values and their fit are represented in red colour. The power-law slope α increases from –0.57 to –0.79 with redshift indicating a steepening of the weak absorber distribution as redshift increases. However, for the high-redshift bin, the Schechter function fails to fit the values towards large equivalent widths where the distribution starts to flatten due to the small number of high-redshift absorbers detected at these equivalent widths.

APPENDIX B: THE COMOVING LINE DENSITY OF O I USING A DIFFERENT COMPLETENESS CORRECTION

One of the reasons for the discrepancy in the dn/dX values between this work and B19 can be associated to the completeness estimates

Table B1. The parameters used in the completeness correction for O I as a function of log N.

z range	T_x	S_x	T_y	S_y
5.32–5.94	−39.76	2.98	1.15	0.38
5.94–6.71	−36.43	2.71	1.16	0.41

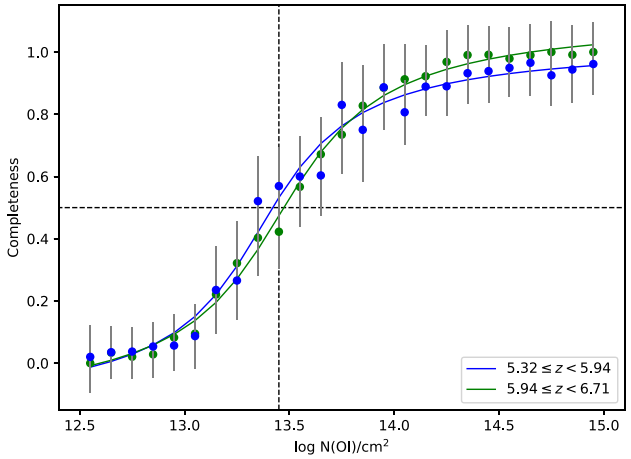

Figure B1. The figure shows the completeness correction for O I as a function of log N.

in B19 where they expect some errors. To understand whether errors in the completeness calculations affect their results, they changed the minimum equivalent width of 25 per cent ($W > 0.05$ Å) used in their analysis. B19 increased the completeness limit to 55 per cent ($W > 1.0$ Å) which reduced the completeness corrections and still were able to recover the upturn in comoving line density at $z > 5.7$, but at lower statistical significance. This is similar to what has been observed in the dn/dX for O I in this work which uses a similar completeness limit of 50 per cent. Therefore, their results seem to be driven by errors in the completeness estimates for smaller values of equivalent width.

The other possible reason for the difference between dn/dX values from our work and B19 might be due to the application of a fixed completeness correction as a function of equivalent width. There is a vague possibility of completeness varying with wavelength (redshift) even outside the masked regions of sky contamination due to changes in the S/N of the spectra at different wavelengths. Also, the completeness for O I depends on the additional lines to be detected (e.g. C II and Si II). If one of these lines remains undetected due to the spectrum being noisy or contaminated at those wavelength regions, then O I would not be identified. Therefore, the dn/dX values from this work are recalculated after applying the completeness correction for O I as a function of column density at different redshift intervals. The obtained values are very similar to the B19 values. However, the dn/dX values obtained by applying completeness corrections as function of W or log N are consistent to each other within the error bars.

The dn/dX for O I is calculated after correcting for completeness using the completeness correction as function of equivalent width. The obtained dn/dX at $z > 5.7$ did not match with the results in B19. In the efforts to figure out the reason behind the discrepancy, the completeness correction for O I is computed as a function of log N at two redshift intervals; $5.32 < z < 5.94$ and $5.94 < z < 6.71$. The

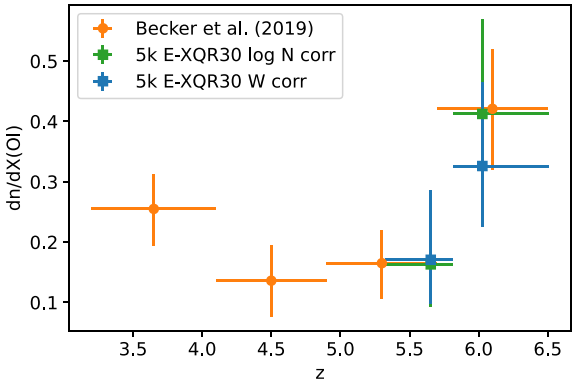

Figure B2. The comoving line density evolution of O I across redshift using a proximity limit of 5000 km s^{-1} and completeness correction as a function of log N is represented in green. The new dn/dX values agree well with the B19 value at $z > 5.7$. The dn/dX values obtained after applying a completeness correction as a function of W are shown in blue. However, both blue and green points at $z > 5.7$ are consistent within the 1σ error bars.

function used to correct for completeness of the sample is as follows:

$$\text{Completeness}(\log N) = S_y(\arctan(S_x W + T_x) + T_y). \quad \text{(B1)}$$

The parameters obtained are given in Table B1.

Fig. B1 shows the new completeness corrections for O I as a function of log N.

The O I absorber data from the catalogue is processed in a similar manner as outlined in Section 2.2. In this case, the 50 per cent completeness limit for O I is log N/cm^2 = 13.45. The dn/dX values obtained after applying the new completeness correction are shown in Fig. B2.

The green squares indicate the values obtained when a completeness correction as a function of column density is applied and blue squares represent the values obtained using the completeness correction as a function of equivalent width. Using the new completeness corrections, the dn/dX values from both works agree to each other in both redshift intervals. However, both values calculated using different completeness corrections are in agreement within the 1σ confidence limits showing that both corrections produce consistent results.

This paper has been typeset from a TEX/LATEX file prepared by the author.